UNIVERSITY OF SOUTHERN CALIFORNIA

DEPARTMENT OF CIVIL ENGINEERING

DIFFRACTION OF P, SV, AND RAYLEIGH WAVES BY SURFACE TOPOGRAPHIES

by

H.L. Wong

Report No. CE 79-05

A Report on Research Conducted Under a Grant from
the United States Geological Survey

Los Angeles, California

January, 1979

TABLE OF CONTENTS

ABSTRACT

A generalized inverse method for boundary conditions is adapted for boundary value problems in elastic wave propagation. Two exact solutions; the first for SH-wave scattering by a semi-cylindrical canyon, and the second for P-wave scattering by a cylindrical cavity are used to test the accuracy of this approximate method. Subsequent applications of this numerical method involve problems not solvable by exact methods, these include the diffraction of P, SV, or Rayleigh waves by irregular surface topographies.

Introduction

In classical seismology, the theoretical models used to compliment the experimental data are usually based on models with simple geometries, the elastic half-space or the layered medium are the most often used. These theoretical models are adequate for studies of long period waves with irregularities smaller than the wavelengths. But recent interests in earthquake engineering and in strong motion seismology have expanded the scope of seismological study to include near field ground motions, where shorter period waves become dominant. The irregular surface topographies or subsurface inhomogeneities can play a major role on the amplification or deamplification at a given site. Moreover, the contribution of soil conditions as observed in recent earthquakes (Jennings, 1971; Sozen, et. al., 1968) to the total motion can no longer be ignored.

As a response to the interests within the field of strong motion seismology, several theoretical investigations were presented to analyze the wave amplification effects. But the progress in analysis is partially stalled by some difficult aspects of the problem: first, the spatial dimensions of the earth's volume is exceptionally large; second, the governing equations for elastic wave propagation are coupled between components; and third, the stress-free boundary which bounds the soil medium poses a much more difficult wave guide problem than those in acoustics and in physics, limiting the number of cases which can be solved exactly.

Perhaps the simplest problems in elastic wave scattering is the two-dimensional SH wave problem. The simplicity is developed from

the acoustic behavior of the SH component, allowing it to be analyzed separately from other body waves. Using basically an image method, exact solutions for SH-wave diffraction problems can be obtained in coordinate systems where the scalar wave equation is separable. Thus far, the cases of a canyon and an alluvial valley with circular (Trifunac, 1971, 1973) or elliptical shapes (Wong and Trifunac, 1974a, 1974b) have been treated.

For the more difficult cases of P or SV incident waves, the mode conversions during reflection or transmission does not permit the use of images, thus, the wave solution is required to satisfy the boundary conditions at the half-space boundary and at the curve boundary simultaneously. Most orthogonal wave functions developed in classical physics are not suitable for these problems. Lee (1978) resolved this difficulty for a hemispherical canyon by expanding the spherical wave functions further into a power series to match all the boundary conditions successfully; the solution procedure, however, leads to a set of infinite matrices which must be solved approximately. Although a similar procedure can be applied for other separable coordinate systems of the wave equation, most problems involving irregular boundaries are treated by approximate numerical methods.

Among the earlier numerical solutions for wave diffraction, the perturbation method has been used to analyse minor irregularities (Asano, 1966; McIvor, 1969), generally, only the first order approximation is retained. Using a similar idea, Aki and Larner (1970) and Bouchon (1975) attacked the problem by assuming the irregularities have shallow slopes and are periodic, the latter assumption enables the problem to be solved by Fourier series. All the restrictions of

small irregularities and shallow slopes can be lifted by using an integral equation method (Wong and Jennings, 1975), formulated with the Green's function of the soil medium. This method was conveniently applied for the study of SH-waves because the Green's function can be derived simply; for more difficult problems, the degree of difficulty is measured by the complexity of the Green's functions.

Other numerical solutions in the field of elastic wave propagation consist of discrete analyses such as the finite difference method (Alterman and Karal, 1968; Boore, 1971; Cherry, 1973) and the finite element method (Smith, 1974; Reimer, et. al., 1974). The detail allowed in these models is theoretically unlimited, but the size of the problem can easily exceed all major computing capabilities. Usually, the real time analyses must be shortened to avoid the reflections from the model boundary. Although Smith (1974) shows that the unwanted boundary reflection can be eliminated from a finite volume analysis by a special algorithm, the effort required increases significantly as the number of ficticious boundaries increases. Nevertheless, from a practical point of view, these discrete methods represent an excellent tool in analyzing the inhomogeneity in the soil.

More recently, several investigators have proposed (Zienkiewicz, 1977a,b,c; Chopra, et. al., 1974) to use the discrete method together with the methods in continuum mechanics. This approach is capable of utilizing the strength of the discrete method (based on a volumial formulation) to analyze the more refined locations near the site and the strength of the continuum mechanics approach (based on a boundary surface formulation) to represent roughly the outgoing waves to the surroundings. This type of approach has the potential of solving many

difficult problems, but the lack of applications in the area of wave propagation can be explained by the difficulty of the continuum solution. Currently, there is no numerical solution in continuum mechanics that is general for two- or three-dimensional elastic wave propagations having a semi-infinite space as a basic model configuration. It is a problem that requires further research.

In this paper, the method of solution applied by Ohsaki (1973) on a static foundation problem will be extended and adapted for dynamic wave propagation problems. This method has been applied (Sanchez-Sesma and Rosenblueth, 1978; England, et. al., 1978) to study SH wave diffraction about a canyon of arbitrary shape, a comparison with exact solution is also made with success. The numerical applications made in this report centers around P, SV, and Rayleigh wave problems, all of which have not been treated extensively in the past because it is difficult to develop admissible solutions that satisfy the stress-free surface of the semi-infinite elastic medium. Using the solution of line sources in a half-space (Lamb, 1904), however, either the wave amplification effects around an arbitrary shaped canyon or the focusing effects within an alluvial valley can be studied simply and accurately. The numerical results as well as the procedures will be described in the following sections.

Description of Ohsaki's Method

In order to obtain an exact and unique solution to an elastodynamic problem, it is well known that both the governing equation and the boundary conditions must be satisfied. Currently, most approximate numerical methods take the approach of first constructing a solution which satisfies approximately the governing equation, then satisfying the boundary conditions at a set of boundary points. This type of approximation is evident in some of the most powerful numerical methods, for example: (1) the finite difference method substitutes the solution of difference equations for that of the original partial differential equations; (2) the finite element method uses the Ritz criteria to construct a solution with shape functions that satisfy only approximately the problem's Euler equation; and (3) the integral equation method substitutes the integral by a discrete sum and forms a matrix equation that approximates the integral equation. All three of these methods match the boundary conditions exactly at a given set of discrete point; other points on the boundary are ignored.

Using Ohsaki's method, however, a different approach is taken by making all approximations with boundary conditions. A function with unknown variables is first chosen to satisfy the governing equation exactly, then the boundary conditions are satisfied in a least-square sense by a generalized inverse method. The advantage of this method is that more attention can be directed at the boundary (where the solution is of interest) rather than at locations far removed from the site.

In setting up a trial solution for the governing equation, the function must be suitable for the problem at hand; perferably, it should satisfy automatically most of the simpler boundary conditions so that the least square approximation of boundary conditions can be reserved for a few difficult locations. In the topographic models studied in this report, the configuration (Figure 1) consists of basically a local irregular topography, Γ, and a flat boundary approximating the distanced topographies. Also, since the earth's volume is extremely large, the x and positive y boundaries are assumed to be infinite. With the geometry of the problem in mind, one suitable basis for the trial function is the line source solution because it satisfies the governing equation exactly except at the source point, and it already accounts for the free surface condition at the half-space surface and the Sommerfeld's radiation conditions at infinity. Therefore, by superimposing several of these line sources, the boundary condition at the irregular surface Γ can be approximated by adjusting the unknown magnitude and phase of the sources, a procedure efficiently performed by the generalized inverse method (Noble, 1969). Physically, the configuration of the model is that of a half-space but the presence of the canyon is ficticiously created by a mathematical trick.

A generalized inverse problem can be set up by defining a matrix [G] so that

$$[G]\{a\} = \{b\} \qquad (1)$$

where {b} is an N-vector which contains the solution function at the N discrete boundary points, {a} is an M-vector which contains the

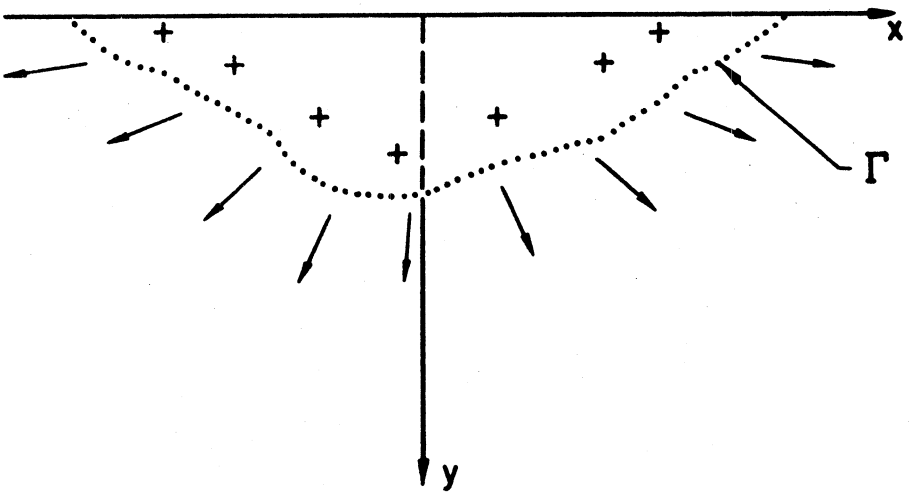

FIGURE 1

complex amplitude of the line sources, and [G] is an N x M matrix which contains the complex solution for unit line sources. The matrix elements of [G] should contain the solution function corresponding to the type of boundary conditions prescribed, i.e., if {b} must match a stress boundary condition {b'}, [G] should contain the stress solution of the line sources.

Since there are usually more conditions than unknowns, {b} cannot match {b'} exactly unless there are (N - M) redundant equations in matrix equation (1). It can be shown (Noble, 1969), however, if {a} is calculated as

$$\{a\} = [G^{*}G]^{-1}[G]^{*}\{b'\} \quad , \tag{2}$$

with the boundary condition being {b} = {b'}; then the square of the error, E, defined as

$$E^{2} = \{b' - b\}^{*}\{b' - b\}$$

will be minimized. The notation $[G]^{*}$ and $\{b' - b\}^{*}$ represents the adjoint (complex conjugate transpose) of [G] and {b' - b}, respectively.

Theoretically, the boundary condition can be matched without any error if equal number of observation points and source points are taken. But a poor placement of these singular sources can cause the solution to be quite poor and unstable at boundary locations other than the prescribed points. The generalized inverse procedure (equation 2) described can give some consideration to additional points on the boundary. Mathematically, the excess of N over M can be considered as extra constraints that create a correction on the solution generated by just M constraints. The magnitude of the correction can be deduced

by partitioning the matrix equation (1) so that

$$\left[\begin{array}{c} G_1 \\ \hline G_2 \end{array}\right] \{a\} = \left\{\begin{array}{c} b_1 \\ \hline b_2 \end{array}\right\} \tag{4}$$

where $[G_1]$ is an M x M minor of [G] having the largest determinant and $\{b_1\}$ is the corresponding right hand vector. The matrix $[G_2]$ and vector $\{b_2\}$ are composed of the remaining (N - M) rows of [G] and {b}, respectively. Since the matrix [G] has a rank of M, $[G_2]$ can be expressed as a linear combination of the rows in $[G_1]$ as

$$[G_2] = [P][G_1] \tag{5}$$

in which [P] is an (N - M) x M matrix.

Using [P], the generalized inverse solution of equation (4) or (1) can be written as

$$[G_1]\{a\} = \{b_1'\} + [I + P^*P]^{-1}[P]^*\{b_2' - Pb_1'\} , \tag{6}$$

where $\{b_2'\}$ and $\{b_1'\}$ are the partitioned vector of the boundary condition

$$\{b'\} = \left\{\begin{array}{c} b_1' \\ \hline b_2' \end{array}\right\} . \tag{7}$$

The solution of {a} in equation (6) is exactly the same as that in equation (2), but it is in a better form to show that the solution {a} can be expressed in two parts

$$\{a\} = \{a_1\} + \{a_2\} \tag{8}$$

where

$$\{a_1\} = [G_1]^{-1}\{b_1'\} \tag{9}$$

is the major part of the solution {a} that matches the most prominant boundary conditions and

$$\{a_2\} = [G_1]^{-1}[I + P^*P]^{-1}[P]^*\{b_2' - Pb_1'\} \tag{10}$$

acts as a correction to the solution {a}. If the correction is relatively large, the trial solution is far from representing the exact solution; but if $\{a_2\}$ is small compared to $\{a_1\}$, the solution is excellent. Moreover, if the (N - M) extra equations

$$[G_2]\{a\} = \{b_2\} \tag{11}$$

of the partitioned matrix equation (4) are redundant with the first M equations, then the vectors $\{b_2'\}$ and $\{b_1'\}$ are related as

$$\{b_2'\} = [P]\{b_1'\} \tag{12}$$

where [P] is defined in equation (5). Consequently, the substitution of equation (12) into equation (10) would render the correction vector $\{a_2\}$ zero.

The procedures described above can be applied to various boundary value problems. Each case requires a matrix similar to [G]. In the following sections, the method will be applied first to two simple problems which have been solved exactly. The first case shall be the diffraction of SH-waves by a cylindrical canyon (Trifunac, 1973), and the second case is the scattering of a plane P-wave by a cylindrical cavity in an infinite space (Mow and Pao, 1971). These examples are to be used as test cases for the accuracy of the method, and also for a feel of how the source locations might be best chosen. Following these examples, the diffraction of P, SV and Rayleigh waves by topographies of arbitrary shape will be studied. Since there are no exact solutions for these latter problems, the accuracy of the numerical method will be judged by the success of the example problems.

Diffraction of SH-Waves From a Semi-Cylindrical Canyon

As one of the few exact solutions available for wave propagation in the geophysics discipline, the solution for wave amplification around a semi-cylindrical canyon subjected to plane incident SH-waves (Trifunac, 1973) is chosen as a test case for Ohsaki's method. In the report by Sanchez-Sesma and Rosenblueth (1978), the numerical results using this method have been performed and compared favorably with the exact solution; it is repeated here with the emphasis placed on the art of choosing a suitable location for the sources. This exercise can be helpful for future application in a more complicated problem where no comparison is possible.

The configuration of the model is shown in Figure 2; the soil medium surrounding the canyon is assumed to be homogeneous and elastic, having a shear wave velocity of β and a shear modulus of μ. The governing equation for the antiplane harmonic displacement, $u_z e^{i\omega t}$, is the scalar Helmholtz equation

$$\frac{\partial^2 u_z}{\partial x^2} + \frac{\partial^2 u_z}{\partial y^2} + k^2 u_z = 0 \qquad (13)$$

where $k = \omega/\beta$ is the wave number. The boundary conditions for a stress-free surface along the entire topography are given as

$$\sigma_{zy} = 0 \quad , \text{ for } |x| > R_o, \; y = 0 \; ; \qquad (14)$$

and

$$\sigma_{zn} = 0 \quad , \text{ for } \sqrt{x^2 + y^2} = R_o \; , \qquad (15)$$

where σ_{zn} is the shear stress identified with the unit normal, $\hat{n}$, at the curve surface Γ. Additional boundary conditions for the boundary at infinity is posed by the Sommerfelt radiation conditions.

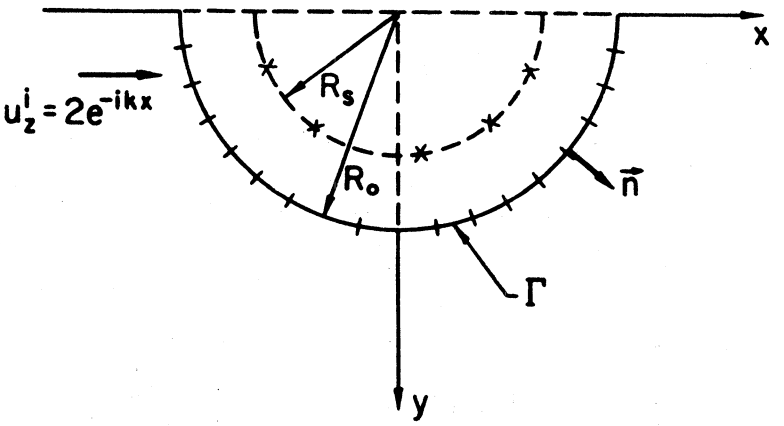

FIGURE 2

Using the principle of superposition, the total displacement field $u_z(x,y)$ can be expressed as

$$u_z(x,y) = u_z^{ff}(x,y) + u_z^{s}(x,y) \quad , \tag{16}$$

where $u_z^{ff}(x,y)$ is the free-field displacement in the half space without the canyon, and $u_z^{s}(x,y)$ is the displacement field of the wave scattered from the canyon. Similarly, the stress fields can be expressed as

$$\sigma(x,y) = \sigma^{ff}(x,y) + \sigma^{s}(x,y) \quad , \tag{17}$$

in which σ^{ff} and σ^{s} are the stresses corresponding to u_z^{ff} and u_z^{s}, respectively. Since the free field motion is usually a given part of the problem, it is convenient to solve the problem with $u_z^{s}(x,y)$, instead of $u_z(x,y)$, as the unknown solution. Thus, the boundary condition for $\sigma_{zn}^{s}(x,y)$ can be introduced as

$$\sigma_{zn}^{s}(x,y) = -\sigma_{zn}^{ff}(x,y), \quad \text{for } \sqrt{x^2+y^2} = R_o \quad , \tag{18}$$

by substituting (17) into (15). Boundary condition (14) remains valid for $\sigma_{zy}^{s}(x,0)$ because $\sigma_{zy}^{ff}(x,0)$ satisfies already that condition.

As indicated in the previous section, the scattered wave motion $u_z^{s}(x,y)$ may be constructed by superimposing the displacement solutions generated by line sources as

$$u_z^{s}(x,y) = \sum_{j=1}^{M} a_j \hat{u}_z(x,y \mid x_j,y_j) \quad , \tag{19}$$

in which the source points (x_j,y_j) are placed within the surface Γ. The line source solution for antiplane displacements in a half-space is simply

$$\hat{u}_z(x,y \mid x_s,y_s) = \frac{i}{4}\left[H_o^{(2)}\left(k\sqrt{(x-x_s)^2 + (y-y_s)^2}\right)\right.$$

$$\left. + H_o^{(2)}\left(k\sqrt{(x-x_s)^2 + (y+y_s)^2}\right)\right] \qquad (20)$$

where $H_o^{(2)}$ is the Hankel's function of second kind and zero order. It is interesting to note that $\hat{u}_z$ satisfies the governing equation

$$\frac{\partial^2 \hat{u}_z}{\partial x^2} + \frac{\partial^2 \hat{u}_z}{\partial y^2} + k^2 \hat{u}_z = -\delta\left(\sqrt{(x-x_s)^2 + (y-y_s)^2}\right), \qquad (21)$$

and therefore satisfies equation (13) at all points except the source points. Furthermore, $\hat{u}_z$ satisfies automatically boundary condition (14) and the Sommerfeld's conditions; the only boundary condition remains to be satisfied is equation (18).

If N observation points (x^i,y^i) are specified on surface Γ, the stresses of the scattered wave can be expressed in a form of a matrix equation as

$$\begin{bmatrix} & \vdots & \\ \cdots\cdots\ \hat{\sigma}_{zn}(x^i,y^i \mid x_j,y_j)\ \cdots\cdots & & \\ & \vdots & \end{bmatrix} \begin{Bmatrix} \vdots \\ a_j \\ \vdots \end{Bmatrix} = \begin{Bmatrix} \vdots \\ \sigma_{zn}{}^s(x^i,y^i) \\ \vdots \end{Bmatrix} \qquad (22)$$

where the matrix elements $\hat{\sigma}_{zn}$ can be calculated from $\hat{u}_z$ through the constitutive equation as

$$\hat{\sigma}_{zn}(x,y \mid x_j,y_j) = \mu \frac{\partial}{\partial n} \hat{u}_z(x,y \mid x_j,y_j) \quad , \qquad (23)$$

or

$$\hat{\sigma}_{zn}(x,y \mid x_j,y_j) = \mu\left[\frac{\partial \hat{u}_z(x,y \mid x_j,y_j)}{\partial x}\left(\frac{\partial x}{\partial n}\right) + \frac{\partial \hat{u}_z(x,y \mid x_j,y_j)}{\partial y}\left(\frac{\partial y}{\partial n}\right)\right] \qquad (24)$$

using the direction cosines, $(\partial x/\partial n,\ \partial y/\partial n)$. Equation (22) is now in the form of equation (1), with the matrix $[\hat{\sigma}]$ and the vector $\{\sigma_{zn}{}^{s}\}$ corresponding to [G] and {b}, respectively. The approximate boundary condition for vector $\{\hat{\sigma}_{zn}{}^{s}\}$ can be obtained from equation (18) as

$$\left\{\begin{array}{c}\vdots\\ \hat{\sigma}_{zn}{}^{s}(x^i,y^i)\\ \vdots\end{array}\right\} \cong \left\{\begin{array}{c}\vdots\\ -\hat{\sigma}_{zn}{}^{ff}(x^i,y^i)\\ \vdots\end{array}\right\} \quad , \tag{25}$$

where $\{-\hat{\sigma}_{zn}{}^{ff}\}$ corresponds to {b'} of equation (2). The next step of the numerical procedure is to calculate the unkowns {a} as

$$\{a\} = [\hat{\sigma}^{*}\hat{\sigma}]^{-1}[\hat{\sigma}]^{*}\{-\sigma_{zn}{}^{ff}\} \quad , \tag{26}$$

then the error

$$E^2 = \left| \sum_{i=1}^{N}\left[\sigma_{zn}{}^{s}(x^i,y^i) + \sigma_{zn}{}^{ff}(x^i,y^i)\right]^2 \right| \tag{27}$$

will be minimized at the N observation points on Γ.

The numerical procedures derived up to this point are applicable for all arbitrary surfaces Γ. The parameters that define the shape of Γ are the N observation points (x^i,y^i), and the direction cosines $(\partial x^i/\partial n,\ \partial y^i/\partial n)$ of the unit normal. For this particular example, the observation points are distributed evenly over the circular arc (Figure 2), and the direction cosines are calculated as

$$\frac{\partial x^i}{\partial n} = \frac{x^i}{R_o}$$

and

$$\frac{\partial y^i}{\partial n} = \frac{y^i}{R_o} \tag{28}$$

In order to compare systematically with the exact solution presented

by Trifunac (1973), the dimensionless frequency

$$\eta = \frac{\omega R_o}{\pi \beta} \tag{29}$$

is defined. It represents physically the ratio of the canyon width to the wavelength of the incident wave. The wave form u_z^{ff} generated by a horizontally propagating SH-wave is also chosen, expressed simply as

$$u_z^{ff}(x,y) = 2e^{-i\pi\eta \frac{x}{R_o}} \tag{30}$$

in which the reflected plane wave from the half space boundary is included.

The major difficulty in applying Ohsaki's method is the lack of a systematic way for placing the source, making the method a trial-and-error type. As an initial attempt, the sources are evently distributed at a circle of radius R_s ($R_s < R_o$), making R_s the only parameter that controls the source locations. Numerically, R_s can be varied until the error E is minimized. But for each assumed value of R_s, a complete recalculation of all matrices and vectors is required, making the guessing type procedures unattractive and uneconomical. Therefore, some numerical experiments must be made to devise a better scheme for placing the source.

In Figures 3a,b,c the error E accumulated at the boundary is plotted versus the radius R_s for $\eta = 0.1$, 1.5, and 4, respectively. In Figures 3a, N is chosen to be 19 points, and 3 sets of solutions calculated with M = 3, 6 and 9 line sources are shown. When M = 3, the radius $R_s = 0.07$ gives the smallest E; while for M = 6 and M = 9, $R_s = 0.3$ and $R_s = 0.5$, respectively, are the optimal source locations. Clearly, the optimal R_s increases as the number of sources increase,

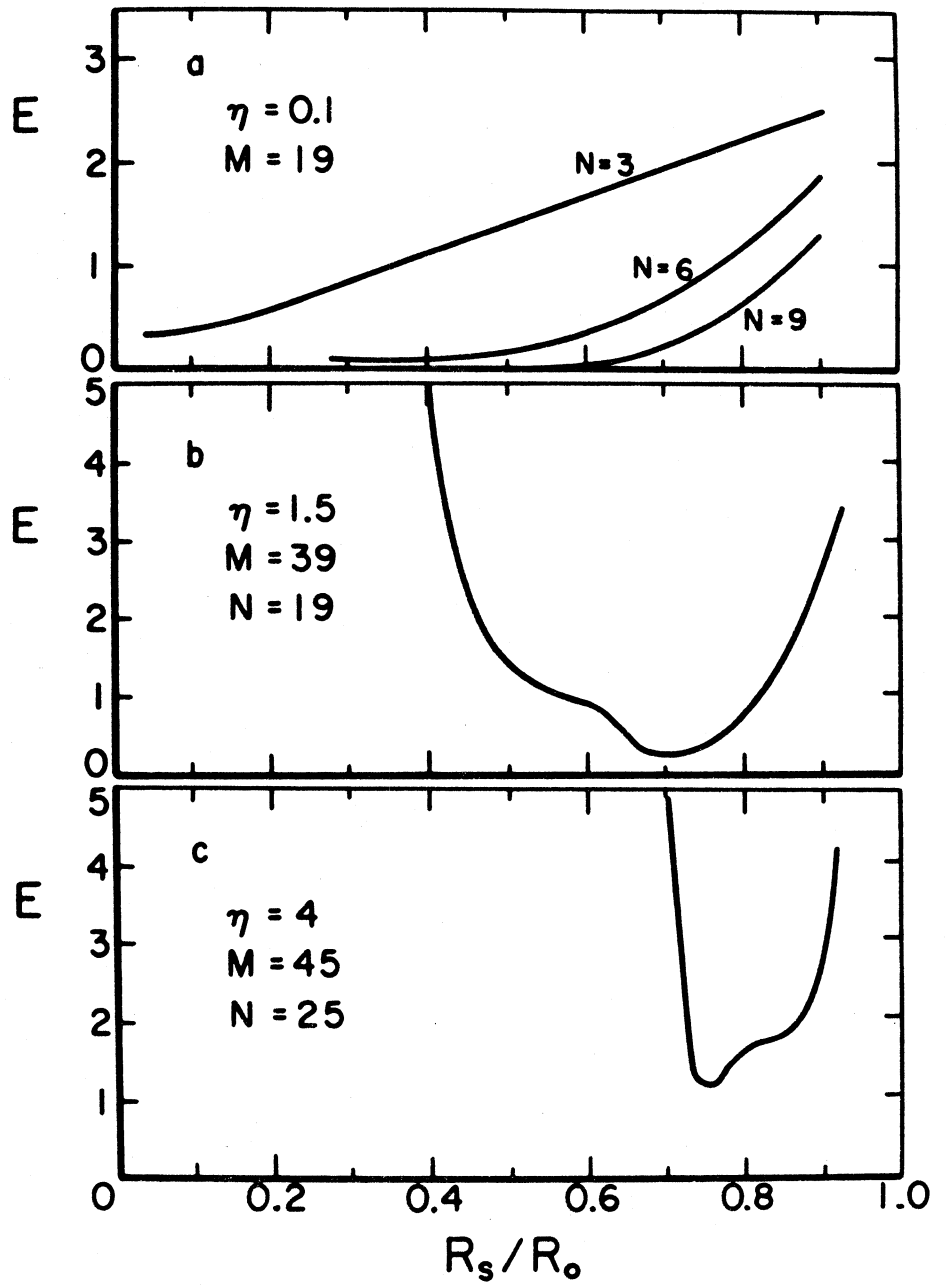

FIGURE 3 Error in Matching of Boundary Conditions as a Function of Source Locations -- Incident SH-Waves

a behavior caused by the "ln R" type singularity of the function $\hat{u}_z$ at the source. If the source is placed very near the boundary, only the boundary conditions close to the source can affect its amplitude and phase, thus, many source points are needed to match all the boundary conditions satisfactorily. On the other hand, when the sources are placed far away from the boundary points, their influences are not too different from one boundary point to another; only a few sources are then needed to balance the boundary points without introducing large errors at certain locations.

If the source locations are chosen with some care, the accumulated error E is usually larger when M is smaller because the minimization procedure has fewer variables. Moreover, for cases with large η, the number of sources must be large and near the surface to handle the rapid variation of the boundary conditions. For example, for the case of $\eta = 1.5$ (Figure 3b), the optimal R_s is 0.7 while for $\eta = 4$ (Figure 3c), the optimal R_s is 0.75.

Using the R_s which yields the least error, the solution of the problem is calculated at locations on the flat surface as well as on the curved surface. The approximate results and the exact solution are tabulated in Table I, II, and III for comparisons. In Table I, three sets of approximate solutions for $\eta = 0.1$ have been made with M = 3, 6 and 9, illustrating the improvement of accuracy as the number of variables increase. For this low frequency case, the results have a relative error of less than 0.1%. In Table II, the results for $\eta = 1.5$ is considered. The approximate results are nearly identical to the exact solution at the locations $|x/R_o| \leq 1$ (on Γ). At the locations $|x| > R_o$, however, the results deteriorate as $|x|$ increases

TABLE I

Comparisons of Approximate Solutions and Exact Solution for $\eta = 0.1$

x/R_o	M = 3 N = 19 $R_s/R_o = 0.07$	M = 6 N = 19 $R_s/R_o = 0.30$	M = 9 N = 19 $R_s/R_o = 0.50$	Exact Series Solution
-4.000	(0.8144,-2.1608)	(0.8152,-2.1614)	(0.8152,-2.1614)	(0.8152,-2.1614)
-3.000	(1.3153,-1.9748)	(1.3160,-1.9756)	(1.3160,-1.9756)	(1.3160,-1.9756)
-2.000	(1.6774,-1.6642)	(1.6779,-1.6649)	(1.6779,-1.6649)	(1.6779,-1.6649)
-1.500	(1.7881,-1.5055)	(1.7885,-1.5054)	(1.7885,-1.5054)	(1.7885,-1.5054)
-1.000	(1.8341,-1.4198)	(1.8339,-1.4176)	(1.8339,-1.4176)	(1.8339,-1.4176)
-0.866	(1.8697,-1.2482)	(1.8696,-1.2493)	(1.8696,-1.2494)	(1.8696,-1.2494)
-0.500	(1.9315,-0.7768)	(1.9318,-0.7810)	(1.9318,-0.7810)	(1.9318,-0.7810)
0.000	(1.9310,-0.1291)	(1.9315,-0.1291)	(1.9310,-0.1291)	(1.9315,-0.1291)
0.500	(1.8318,0.5184)	(1.8318,0.5227)	(1.8318,0.5227)	(1.8318,0.5227)
0.866	(1.6968,0.9897)	(1.6964,0.9908)	(1.6964,0.9909)	(1.6964,0.9909)
1.000	(1.6343,1.1612)	(1.6339,1.1590)	(1.6339,1.1590)	(1.6339,1.1590)
1.500	(1.5746,1.2497)	(1.5741,1.2495)	(1.5741,1.2495)	(1.5741,1.2495)
2.000	(1.4371,1.4157)	(1.4366,1.4163)	(1.4366,1.4163)	(1.4365,1.4163)
3.000	(1.0184,1.7515)	(1.0177,1.7523)	(1.0177,1.7523)	(1.0177,1.7523)
4.000	(0.4736,1.9741)	(0.4728,1.9747)	(0.4728,1.9747)	(0.4728,1.9747)

TABLE II

Comparisons of Approximate Solution and Exact Solution for $\eta = 1.50$

x/R_o	M = 19 N = 39 $R_s/R_o = 0.70$	Exact Series Solution
-4	(1.2767,0.0854)	(0.8950,-0.5536)
-3	(-0.1091,-2.8517)	(0.4416,-2.1918)
-2	(-0.9053,-0.1618)	(-0.8823,-0.1026)
-1.5	(0.3092,-2.2048)	(-0.3101,-2.2105)
-1.25	(0.5239,1.6137)	(0.5240,1.6142)
-1	(0.3744,3.8841)	(0.3744,3.8842)
-0.74	(-3.3682,1.6040)	(-3.3684,1.6040)
0.48	(-2.4298,-2.3578)	(-2.4299,-2.3577)
0.25	(0.9337,-2.9987)	(0.9338,-2.9988)
0.0	(2.6437,-0.2424)	(2.6436,-0.2423)
0.25	(0.6820,2.1094)	(0.6820,2.1094)
0.48	(-1.4517,1.1300)	(-1.4516,1.1299)
0.74	(-0.2704,-1.1884)	(-0.2702,-1.1885)
1	(-0.4726,0.8769)	(-0.4727,0.8767)
1.25	(-0.7771,0.7310)	(-0.7770,0.7305)
1.5	(-1.1508,0.0743)	(-1.1499,0.0710)
2	(0.2184,-1.2552)	(0.2414,-1.3144)
3	(-1.3252,0.4632)	(-0.7745,-0.1966)
4	(0.8136,1.2307)	(0.4319,1.8697)

TABLE III

Comparisons of Approximate Solution and Exact Solution for $\eta = 4.00$

x/R_o	M = 25 N = 45 $R_s/R_o = 0.75$	Exact Series Solution
-4.00	(2.7570,-0.0401)	(2.9935,-0.4792)
-3.00	(2.8928,-0.0462)	(2.4720,-0.1624)
-2.00	(3.1457,-0.0640)	(3.3787,0.4276)
-1.50	(3.4018,-0.0893)	(3.0935,-0.5348)
-1.25	(-3.6209,0.1112)	(-3.6668,0.0168)
-1.00	(3.9782,-0.1514)	(3.9755,-0.1624)
-0.76	(-3.8716,0.5306)	(-3.8613,0.5198)
-0.54	(3.0761,-2.0956)	(3.0764,-2.1135)
-0.28	(-2.9419,1.6120)	(-2.9507,1.6000)
0.00	(2.7347,-0.1153)	(2.7325,-0.1156)
0.28	(-1.6208,-1.1498)	(-1.6221,-1.1355)
0.54	(0.2574,1.3129)	(0.2551,1.3210)
0.76	(0.4609,-0.7904)	(0.4722,-0.7857)
1.00	(-0.3355,0.3873)	(-0.3417,0.3964)
1.25	(-0.6133,-0.0881)	(-0.6591,0.0060)
1.50	(0.3763,-0.6214)	(0.0674,-0.1755)
2.00	(-0.6062,-0.6174)	(-0.3732,-1.1091)
3.00	(-0.9201,0.4266)	(-1.3406,0.9577)
4.00	(-0.5681,0.9419)	(-0.3312,1.3809)

because this approximate method is designed for locations near the boundary.

The largest source of error for the solution at large distances is caused by the phase errors of the sources. For the exact solution, the reflected waves originate from the surface Γ while in Ohsaki's approach, the reflected waves are generated at points within the boundary. Hence, the combined phase error of all M sources can be quite large at long distances. The only way to eliminate this problem is to put the sources close to the surface and increase M at the same time, then the solution would improve even at large distances.

In Table III the high frequency case, $\eta = 4$, is compared. At this high frequency, the numerical task is difficult even for computing the exact series solution. Nevertheless, the approximate solution still compares favorably for $|x/R_o| \leq 1$. The numerical errors of the approximate solution seem to be most prominant when either the real or imaginary part is much smaller than the other; this type of error is natural for most complex solutions when the number of significant digits is limited. At large distances and at high frequencies, the approximate solution is usually not reliable due to the phase errors, but the amplitude, $|u|$, approaches that of the exact solution because the solution of the line source (equation (20)) attenuates in the same way as the exact solution.

Besides the results obtained by placing the sources on a concentric cricle, several other experiments with source locations have been performed with marginally improved solutions. Although there are many combinations of trial functions possible, it is not cost effective

to spend a lot of time hunting for the best solution; rather the number of source points and observation points should be large enough to describe the problem. Roughly, N should be 10 points per wavelength, and the number of sources can be about 2/3 of N. In the next section, more numerical examples will be performed on a plane strain problem where the number of variables is increased by a factor of 2.

Diffraction of P Waves by a Cylindrical Cavity

In this section, the solution for P-wave diffraction by a cylindrical cavity (Mow and Pao, 1971) is chosen as a standard for comparison with Ohsaki's method. Unlike SH-waves, the diffraction of P-waves is coupled with SV-waves for most circumstances, making the problem mathematically and physically more difficult to describe. To date, very few analytical investigations have dealt with the scattering of P or SV-waves by irregular objects. Therefore, if Ohsaki's method can be proven satisfactory, it can be used to solved many previously unsolved problems.

Consider now the model shown in Figure 4. The infinite space is assumed to be homogeneous and elastic, having a compressional wave velocity of α and a shear wave velocity of β. The stiffness of the material can be described by λ and μ, the Lamé constants. The boundary conditions of the problem are such that the normal stress σ_{nn} and the tangential stress σ_{nt} at the cavity surface must vanish; but they can be rearranged as

$$\sigma_{nn}{}^{s}(x,y) = - \sigma_{nn}{}^{ff}(x,y) \quad , \qquad \text{for } \sqrt{x^2 + y^2} = R_o \ , \tag{31}$$

and

$$\sigma_{nt}{}^{s}(x,y) = - \sigma_{nt}{}^{ff}(x,y) \quad , \qquad \text{for } \sqrt{x^2 + y^2} = R_o \ , \tag{32}$$

respectively, if the total stress σ is assumed to be the sum of the stress induced by the free-field motion σ^{ff} and the stress of the scattered wave σ^{s}.

Since there are no other boundary conditions other than the Sommerfeld's radiation conditions, the conditions of equations (31)

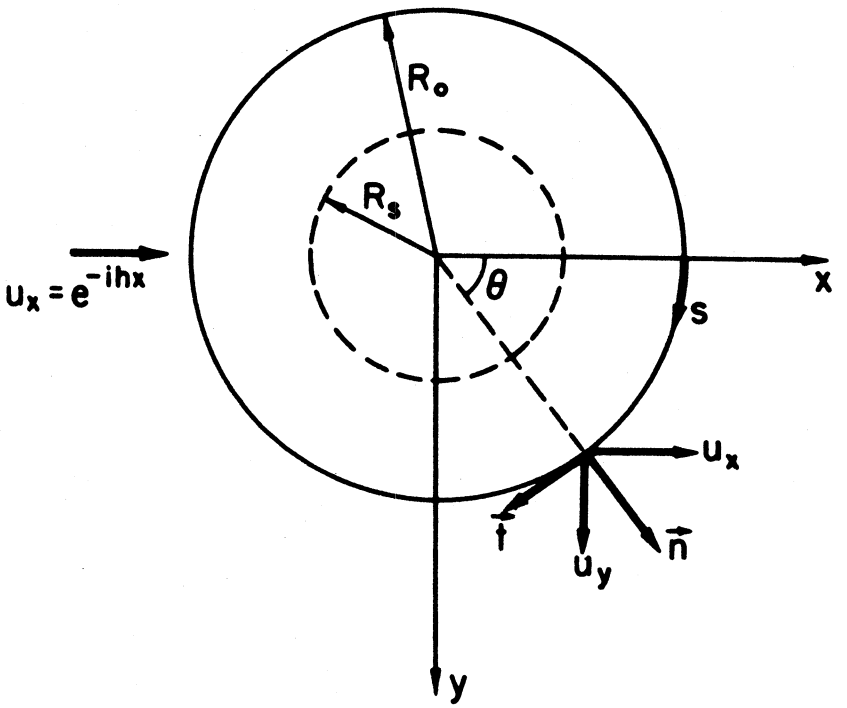

FIGURE 4

and (32) may be satisfied by a generalized inverse procedure. The proposed solution for the scattered wave is again constructed from the line source solutions, but the inplane displacements $u_x(x,y)$ and $u_y(x,y)$ are governed by a set of coupled equations that are difficult to resolve. Therefore, it is convenient to introduce the potentials ϕ and ψ, so that the vector wave equation can be separated as

$$\frac{\partial^2\phi}{\partial x^2} + \frac{\partial^2\phi}{\partial y^2} + h^2\phi = 0 \quad , \tag{33}$$

and

$$\frac{\partial^2\psi}{\partial x^2} + \frac{\partial^2\psi}{\partial y^2} + k^2\psi = 0 \quad , \tag{34}$$

where $h = \omega/\alpha$ and $k = \omega/\beta$ are wave numbers for P and SV waves, respectively. Using the potentials, the displacements, u_x and u_y, can be expressed as

$$u_x = \frac{\partial\phi}{\partial x} + \frac{\partial\psi}{\partial y} \quad , \tag{35}$$

and

$$u_y = \frac{\partial\phi}{\partial y} - \frac{\partial\psi}{\partial x} \quad . \tag{36}$$

Similarly, the stresses can be derived directly from the potentials as

$$\frac{1}{\mu}\sigma_{xx} = -k^2\phi - 2\frac{\partial^2\phi}{\partial y^2} + 2\frac{\partial^2\psi}{\partial x\partial y} \quad , \tag{37}$$

$$\frac{1}{\mu}\sigma_{yy} = -k^2\phi - 2\frac{\partial^2\phi}{\partial x^2} - 2\frac{\partial^2\psi}{\partial x\partial y} \quad , \tag{38}$$

and

$$\frac{1}{\mu}\sigma_{xy} = 2\frac{\partial^2\phi}{\partial x\partial y} - k^2\psi - 2\frac{\partial^2\psi}{\partial x^2} \tag{39}$$

Using the above expressions, the basis for the trial solution can be composed of line source solutions for equations (33) and (34), they are respectively,

$$\hat{\phi}(x,y \mid x_s,y_s) = H_o^{(2)}\left(h\sqrt{(x-x_s)^2+(y-y_s)^2}\right), \tag{40}$$

and

$$\hat{\psi}(x,y \mid x_s,y_s) = H_o^{(2)}\left(k\sqrt{(x-x_s)^2+(y-y_s)^2}\right), \tag{41}$$

The expression in equation (40) represents a compressional wave source while expression (41) represents an equivolumial source. Both $\hat{\phi}$ and $\hat{\psi}$ must be used to form the trial solution because the diffraction of a P or SV wave by a curved boundary guarantees mode conversion. Thus, if M sources of each type are superimposed, the displacement field of the scattered wave can be expressed as

$$u^s(x,y) = \sum_{j=1}^{M}\left[c_j\hat{u}^{\phi}(x,y \mid x_j,y_j) + d_j\hat{u}^{\psi}(x,y \mid x_j,y_j)\right] \tag{42}$$

where c_j and d_j are the unknown complex amplitudes, $\hat{u}^{\phi}$ and $\hat{u}^{\psi}$ are the displacements generated by the sources $\hat{\phi}$ and $\hat{\psi}$, respectively. Equation (42) holds true for either u_x or u_y. For the purpose of mathcing boundary conditions, the expression for a general component of stress can be written as

$$\hat{\sigma}^s(x,y) = \sum_{j=1}^{M}\left[c_j\hat{\sigma}^{\phi}(x,y \mid x_j y_j) + d_j\hat{\sigma}^{\psi}(x,y \mid x_j,y_j)\right], \tag{43}$$

where $\hat{\sigma}^{\phi}$ and $\hat{\sigma}^{\psi}$ are stresses corresponding to $\hat{\phi}$ and $\hat{\psi}$, respectively. The ten quantities used in equations (42) and (43), i.e., $\hat{u}_x^{\phi}$, $\hat{u}_y^{\phi}$,

$\hat{\sigma}_{xx}^{\phi}$, $\hat{\sigma}_{yy}^{\phi}$, $\hat{\sigma}_{xy}^{\phi}$, $\hat{u}_x^{\psi}$, $\hat{u}_y^{\psi}$, $\hat{\sigma}_{xx}^{\psi}$, $\hat{\sigma}_{yy}^{\psi}$, and $\hat{\sigma}_{xy}^{\psi}$, can be derived by substituting either equation (40) or (41) into equations (35) through (39). Their expressions are compiled in Appendix A for reference.

To match boundary conditions for a surface that does not fit the Cartesian coordinates, stress transformations from σ_{xx}, σ_{yy}, and σ_{xy} to σ_{nn} and σ_{nt} can be applied. If the direction cosines of the unit normal $\hat{n}$ are $\cos\theta$ and $\sin\theta$, then the stresses are related as (Fung, 1965)

$$\sigma_{nn} = \sigma_{xx}\cos^2\theta + \sigma_{yy}\sin^2\theta + 2\sigma_{xy}\sin\theta\cos\theta \ , \tag{44}$$

and

$$\sigma_{nt} = (-\sigma_{xx} + \sigma_{yy})\sin\theta\cos\theta + \sigma_{xy}(\cos^2\theta - \sin^2\theta) \ , \tag{45}$$

These two expressions are necessary for matching boundary conditions (31) and (32).

By specifying N observation points (x^i,y^i) on the cavity surface, the stress field of the scattered wave can be expressed as a matrix product

$$\begin{bmatrix} \vdots & \vdots \\ \cdots\ \hat{\sigma}_{nn}^{\phi}(x^i,y^i|x_j,y_j)\ \hat{\sigma}_{nn}^{\psi}(x^i,y^i|x_j,y_j)\ \cdots \\ \cdots\ \hat{\sigma}_{nt}^{\phi}(x^i,y^i|x_j,y_j)\ \hat{\sigma}_{nt}^{\psi}(x^i,y^i|x_j,y_j)\ \cdots \\ \vdots & \vdots \end{bmatrix} \begin{Bmatrix} \vdots \\ c_j \\ d_j \\ \vdots \end{Bmatrix} = \begin{Bmatrix} \vdots \\ \sigma_{nn}^{s}(x^i,y^i) \\ \sigma_{nt}^{s}(x^i,y^i) \\ \vdots \end{Bmatrix} \tag{46}$$

in which equations (43) through (45) were applied. The next step is to introduce the approximate boundary condition for $\{\sigma^s\}$, it can be accomplished by quantizing equations (31) and (32) as

$$\begin{Bmatrix} \vdots \\ \sigma_{nn}{}^{s}(x^i,y^i) \\ \sigma_{nt}{}^{s}(x^i,y^i) \\ \vdots \end{Bmatrix} \cong \begin{Bmatrix} \vdots \\ -\sigma_{nn}{}^{ff}(x^i,y^i) \\ -\sigma_{nt}{}^{ff}(x^i,y^i) \\ \vdots \end{Bmatrix} . \tag{47}$$

The remainder of the procedures follows as before, except the matrix equation (46) has 2M equations and 2N unknowns, twice the size of the SH problem.

The specification of the free-field motion is straight forward for this problem because there is no extra reflection from a stress free half-plane. The displacement fields of a plane compressional wave traveling in the x-direction are

$$u_x{}^{ff}(x,y) = e^{-ihx} , \tag{48}$$

and

$$u_y{}^{ff}(x,y) = 0 . \tag{49}$$

The corresponding stresses in Cartesian coordinates are

$$\frac{1}{\mu}\sigma_{xx}{}^{ff}(x,y) = -\frac{ik^2}{h}e^{-ihx} , \tag{50}$$

$$\frac{1}{\mu}\sigma_{yy}{}^{ff}(x,y) = -\frac{i}{k}[k^2 - 2h^2]e^{-ihx} , \tag{51}$$

and

$$\frac{1}{\mu}\sigma_{xy}{}^{ff}(x,y) = 0 . \tag{52}$$

The stresses $\sigma_{nn}{}^{ff}$ and $\sigma_{nt}{}^{ff}$ required for equation (47) may be obtained by substituting (50), (51) and (52) into equations (44) and (45).

Borrowing the idea from the previous example, the sources are again distributed evenly on a concentric circle R_s ($R_s < R_o$) within

the circular boundary as shown in Figure 4. Various values of R_s are attempted to get as small a value of E as possible; the relationship of E versus R_s is shown in Figure 5a for $\eta = 0.5$ and in Figure 5b for $\eta = 1$. Generally, the same type of conclusions can be made as before. They are:

(i) For a large number of sources, the sources must be placed closer to the scatterer's surface.

(ii) The error, E, accumulated in matching the boundary conditions, decreases as the number of sources increases.

(iii) For the same number of sources, E increases as the dimensionless frequency η increases.

The accuracy of the numerical solution is again excellent as indicated by the values shown in Table IV, where the radial component of displacement,

$$u_r(R_o,\theta) = u_x\cos\theta + u_y\sin\theta \tag{56}$$

is compared for $\eta = 0.5$. Three sets of approximate solutions calculated with $M = 29$ observation points and $N = 8$, 16 and 24 source points (2 unknowns per point) are presented with the exact solution. It is clear that the approximate solution is excellent for the case with $N = 24$, but even for $N = 8$, the approximate values are adequate for most applications. It is interesting to note that the optimal R_s is different (0.09, 0.3, 0.49) for each value of N, being consistent with the conclusions above. Two other sets of numerical comparisons are shown in Table V and VI for $\eta = 1$ and $\eta = 2$, respectively. The overall results match remarkably well, giving a vote of confidence to Ohsaki's method as a tool for more difficult wave diffraction problems.

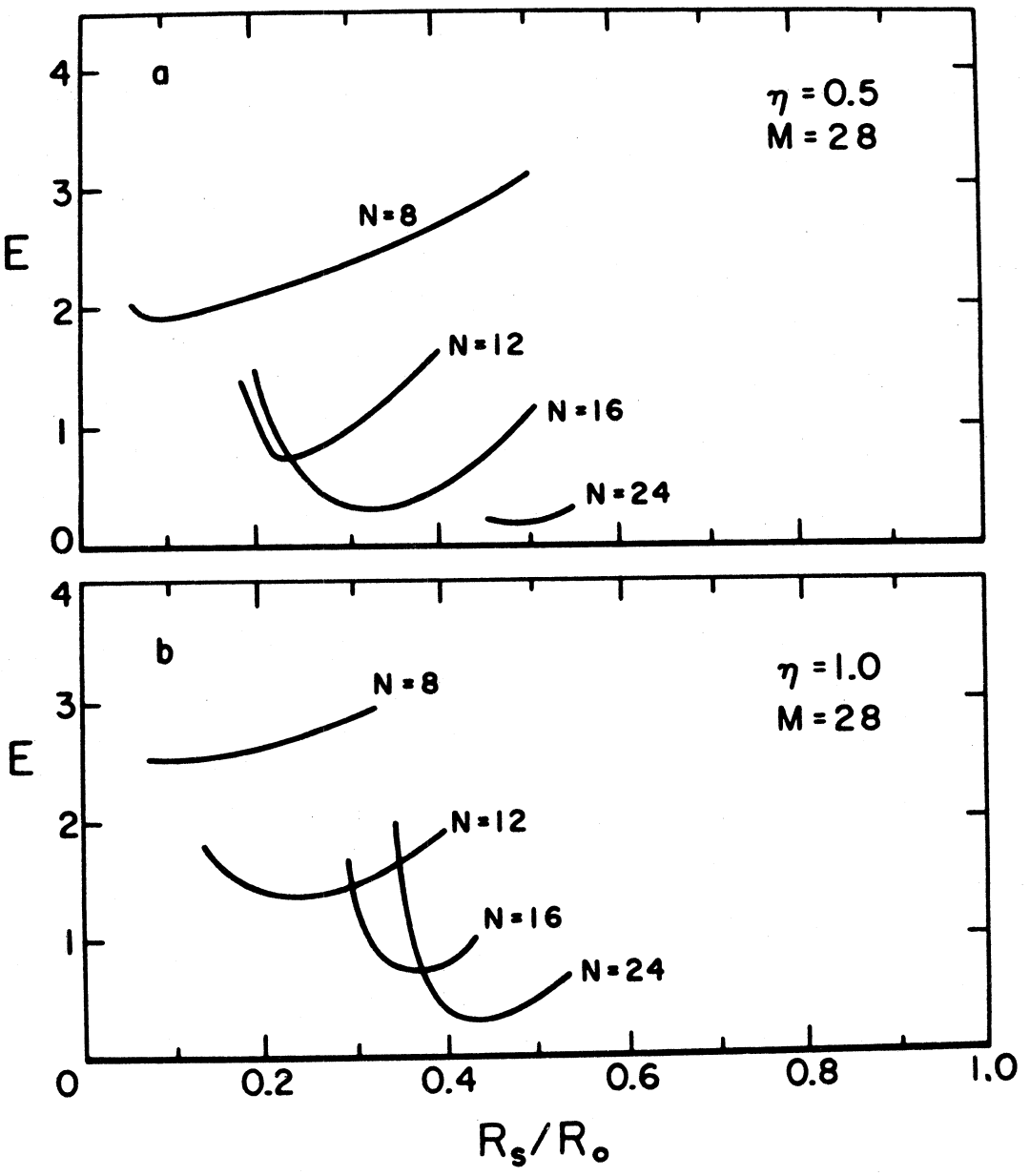

FIGURE 5 Error in Matching of Boundary Conditions as a Function of Source Locations -- Incident P-Waves

TABLE IV

Comparison of Approximate Solutions with the Exact Solution

DISPLACEMENT COMPONENT $u_r = u_x \cos\theta + u_y \sin\theta$

θ	$\eta = 0.50$ M = 28 N = 8 $R_s/R_o = 0.09$	$\eta = 0.50$ M = 28 N = 16 $R_s/R_o = 0.3$	$\eta = 0.50$ M = 28 N = 24 $R_s/R_o = 0.49$	Exact Series Solution
0	(-0.634,0.342)	(-0.700,0.239)	(-0.700,0.238)	(-0.700,0.238)
$\pi/7$	(-0.511,0.316)	(-0.517,0.303)	(-0.517,0.303)	(-0.517,0.303)
$2\pi/7$	(-0.305,0.248)	(-0.234,0.335)	(-0.235,0.334)	(-0.235,0.334)
$3\pi/7$	(-0.352,0.212)	(-0.311,0.241)	(-0.311,0.241)	(-0.311,0.241)
$4\pi/7$	(-0.717,0.390)	(-0.766,0.343)	(-0.766,0.344)	(-0.766,0.344)
$5\pi/7$	(-1.092,0.879)	(-1.169,0.852)	(-1.170,0.851)	(-1.170,0.851)
$6\pi/7$	(-1.288,0.417)	(-1.284,1.463)	(-1.284,1.463)	(-1.284,1.463)
π	(-1.345,1.638)	(-1.274,1.727)	(-1.273,1.729)	(-1.274,1.729)

TABLE V

Comparison of Approximate Solutions with the Exact Solution

DISPLACEMENT COMPONENT $u_r = u_x\cos\theta + u_y\sin\theta$

θ	$\eta = 1.00$ $M = 28$ $N = 16$ $R_s/R_o = 0.35$	Exact Series Solution
0	(0.054,-0.405)	(0.056,-0.401)
$\pi/7$	(-0.146,-0.276)	(-0.144,-0.281)
$2\pi/7$	(-0.258,-0.003)	(-0.261,-0.001)
$3\pi/7$	(-0.291, 0.121)	(-0.289, 0.122)
$4\pi/7$	(-0.665, 0.394)	(-0.667, 0.393)
$5\pi/7$	(-0.727, 1.176)	(-0.727, 1.179)
$6\pi/7$	(-0.248, 1.873)	(-0.246, 1.870)
π	(-0.045, 2.081)	(-0.043, 2.083)

TABLE VI

Comparison of Approximate Solutions with the Exact Solution

DISPLACEMENT COMPONENT $u_r = u_x\cos\theta + u_y\sin\theta$

θ	$\eta = 2.00$ $M = 28$ $N = 20$ $R_s/R_o = 0.45$	Exact Series Solution
0	(-0.049, 0.263)	(-0.054, 0.264)
$\pi/7$	(0.129, 0.014)	(0.133, 0.011)
$2\pi/7$	(0.048,-0.354)	(0.046,-0.353)
$3\pi/7$	(-0.359,-0.145)	(-0.360,-0.144)
$4\pi/7$	(-0.534, 0.567)	(-0.534, 0.566)
$5\pi/7$	(0.504, 1.213)	(0.502, 1.217)
$6\pi/7$	(1.756, 0.540)	(1.759, 0.538)
π	(2.030,-0.004)	(2.028, 0.001)

Diffraction of P or SV Waves by an Elliptical Canyon

Since the accuracy of Ohsaki's method has been proven to be adequate for dimensionless frequencies as high as $\eta = 2$, it can be applied with confidence to analyze the diffraction pattern of P or SV waves by a canyon of arbitrary shape. The configuration of the present model is shown in Figure 6. The canyon surface, without any loss in generality, is assumed to be semi-elliptical in shape, having a major axis of R_o and a minor axis of R_1. This particular shape of the canyon is chosen mainly for its simplicity and partly for its flexibility in varying the canyon depth. Furthermore, the amplification of SH waves surrounding a semi-elliptical canyon (Wong and Trifunac, 1974b) has been analyzed exactly by a series solution, it would be appropriate to study the major differences between the antiplane motions and the inplane motions. It is possible that the physical phenomena of wave diffraction are entirely different for the two cases even though the geometry of the canyon is the same.

To obtain the solution of this problem, the techniques developed by the previous examples are required. In the first example, the problem has a geometry very similar to the present one, but the type of waves studied were antiplane. In the second example, the wave type is plane strain but an infinite space is used instead of a half space, simplifying considerably the boundary conditions of the problem. Using the similarities that exist between the current problem and the previous examples, most of the equations derived in the previous sections can be re-used. The parts that need major revision are the line source solutions and the free-field motions,

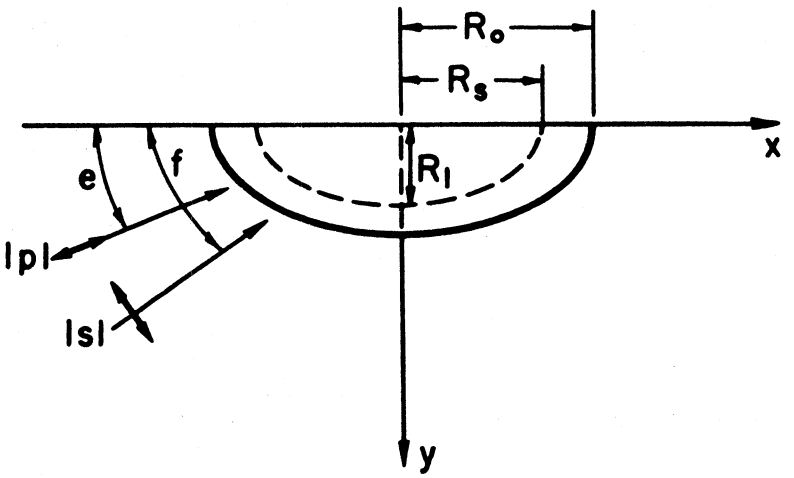

FIGURE 6

both of which must satisfy independently the boundary conditions,

$$\sigma_{yx}(x,0) = 0 \quad , \tag{57}$$

and

$$\sigma_{yy}(x,0) = 0 \quad , \quad \text{for} \quad |x| \geq R_o \quad , \tag{58}$$

at the half space boundary

Since the free-field motion, $u^{ff}(x,y)$, for incident waves is defined using a half-space configuration, the boundary conditions (57) and (58) can be matched quite simply (Ewing, et. al., 1957). The pattern of wave amplification, however, is not trivial because the reflection from the boundary usually includes both P and SV waves, except for a few special cases. The necessary displacement and stress fields for the current problem are displayed in Appendix C.

In order to form a scattered wave solution, $u^s(x,y)$, that satisfies the boundary conditions in equations (57) and (58), the line source solutions to be used must also satisfy them. Unlike the antiplane solution, the superposition of an image can eliminate only one of the two stresses required. For example, an image source can eliminate the shear stress, σ_{yx}, for a compressional source and the normal stress, σ_{yy}, for a shear source. The remaining stress component at the half plane can be eliminated by superimposing an equal and opposite stress distribution, expressed usually in a form of an infinite integral (Lamb, 1904). Thus, the expressions for $\hat{\phi}$, $\hat{\psi}$, $\hat{\sigma}$, and $\hat{u}$ are all infinite integrals, all of which are presented in Appendix B. The numerical evaluation of these line source solutions is by far the most difficult part of the entire numerical procedure.

It requires some complex contour integrations to evaluate these integrals numerically because of the Rayleigh Pole in the functions. Physically, the residue of the Rayleigh Pole represents the Rayleigh surface waves.

Since the line source solutions in Appendix B satisfy already the boundary conditions (57), (58), and the Sommerfeld's radiation conditions, the boundary conditions at the canyon surface is the only one that needs to be matched in the least square sense. The boundary conditions of equations (31) and (32) applies also for the present problem, therefore, procedures developed from equations (42) through (47) can be applied once again. Overall, there are only two major revisions of the procedure:

(i) Replace the expressions for the free-field motion in equations (48) through (52) by the expressions in Part (1) of Appendix C for P wave incidence and those in Part (2) of Appendix C for SV wave incidence.

(ii) Use the expressions for $\hat{\phi}$, $\hat{\psi}$, $\hat{u}$, and $\hat{\sigma}$ in Appendix B instead of Appendix A because the boundary conditions (57) and (58) must be satisfied.

After the above changes, the procedure follows immediately.

The parameters to be used for the studies in this section are η, the dimensionless frequency, R_1/R_o, the ratio of the depth of the canyon to its width, e, the angle of P wave incidence (Figure C1), and f, the angle of SV wave incidence (Figure C2). Once again, the approximate solutions are obtained by locating the source points on an elliptical contour within the canyon boundary; its major axis is R_s. The observation points on the canyon surface are distributed

evenly in the parameter θ, which defines the elliptical surface as

$$x(\theta) = R_o \cos\theta \tag{59}$$

and

$$y(\theta) = R_1 \sin\theta \ . \tag{60}$$

Before proceeding with the actual numerical work, it is important to perform some checking on the convergence rate of the solutions. Although there are no exact solutions available for comparison, the checking can be performed by comparing the approximate solution calculated by a different number of source points and observation points. The solutions can be considered convergent if the results improve as the number of variables increases.

Tabulated in Tables VII and VIII are the approximate solutions for the amplitude of u_y induced by a vertically incident P wave. They will be used for the convergence comparison. The dimensionless frequencies used are $\eta = 1.00$ and $\eta = 2.00$ for Tables VII and VIII, respectively. The numerical solutions were calculated by taking 22 observation points and a varying number of source points as N = 7, 9, and 15. Since the case with N = 15 accumulates the least error in the boundary condition matching procedures, it will be used as the basis for the comparison. Hence, the error ε placed next to the solutions with N = 10 and N = 7 are the relative error calculated using the corresponding "N = 15" solutions. It is clear that the error for the solution using N = 10 is generally lower than that using N = 7, showing a convergent trend. The maximum error, however, does not always occur at the same location of x/R_o because of the different

TABLE VII

A Comparison Between Approximate Solutions
Values of $|u_y|$ for $\eta = 1.00$, M = 22, and e = 90°

x/R_o	N=15	N=10	ε	N=7	ε
1.000	2.514	2.392	5%	2.325	7.5%
0.989	2.420	2.324	4%	2.239	7.5%
0.956	2.121	2.076	2%	2.006	5.4%
0.901	1.725	1.737	0.7%	1.685	2%
0.826	1.407	1.453	3%	1.401	0.4%
0.733	1.377	1.404	2%	1.312	4.7%
0.623	1.615	1.608	0.4%	1.475	8.5%
0.500	1.922	1.913	0.5%	1.802	6%
0.365	2.193	2.197	0.2%	2.166	1%
0.223	2.387	2.393	0.3%	2.455	3%
0.075	2.489	2.479	0.4%	2.605	4.7%

TABLE VIII

A Comparison Between Approximate Solutions
Values of $|u_y|$ for $\eta = 2.00$, M = 22, and e = 90°

x/R_o	N=15	N=10	ε	N=7	ε
1.000	2.477	2.495	0.7%	2.386	3.7%
0.989	2.124	2.150	1.2%	2.056	3%
0.956	1.287	1.336	3.8%	1.299	0.9%
0.901	1.049	0.981	6.5%	0.828	21%
0.826	1.695	1.632	3.7%	1.450	14%
0.733	2.123	2.184	3%	2.113	0.5%
0.623	2.240	2.315	3%	2.376	6%
0.500	2.232	2.156	3.4%	2.290	2.6%
0.365	2.168	2.024	6.6%	2.106	3%
0.233	2.087	2.067	1%	2.038	2.3%
0.075	2.030	2.158	6%	2.066	1.8%

source positions for each case. Using the discussion made by equations (4) through (12), the observation points near the sources have a strong influence on the solution; other points are used mainly as corrections.

The all-important factor for the placement of sources is again studied; the error E is calculated for various source radii, R_s, and is plotted in Figure 7 for $\eta = 1.0$ and $\eta = 2.0$. The behavior of the "E vs. R_s" curves are quite similar to those encountered in the previous sections, having the optimal R_s/R_o between 0.4 and 0.6 for nearly all cases. The analyses made in this section are calculated with $R_s/R_o = 0.4$ for $\eta = 0.5$ or lower, and with $R_s/R_o = 0.5$ for higher values of η. The number of observation points used is 22 (2 components per point) and the number of source points is 15 for all cases.

Consider the first amplification of P-waves around a circular canyon. The amplitudes of $|u_x|$ and $|u_y|$ are plotted as a function of x/R_o for $\eta = 0.25$, 0.50, 0.75, 1.00, 1.50 and 2.00 in Figures 8 through 13. In each figure, the effects of the incidence wave angle e = 30°, 60° and 90° are shown. It is important to note that the free field amplitudes for P-waves are

$$|u_x^{ff}| = 1.39 \quad , \quad |u_y^{ff}| = 1.12 \quad , \text{ for } e = 30° \ ,$$

$$|u_x^{ff}| = 0.96 \quad , \quad |u_y^{ff}| = 1.74 \quad , \text{ for } e = 60° \ ,$$

$$|u_x^{ff}| = 0.00 \quad , \quad |u_y^{ff}| = 2.00 \quad , \text{ for } e = 90° \ ,$$

so that the deviation of wave amplitudes caused by a canyon can be judged. Generally, the amplifications of $|u_x|$ and $|u_y|$ by a circular canyon topography are always less than 2 times the free field amplitudes.

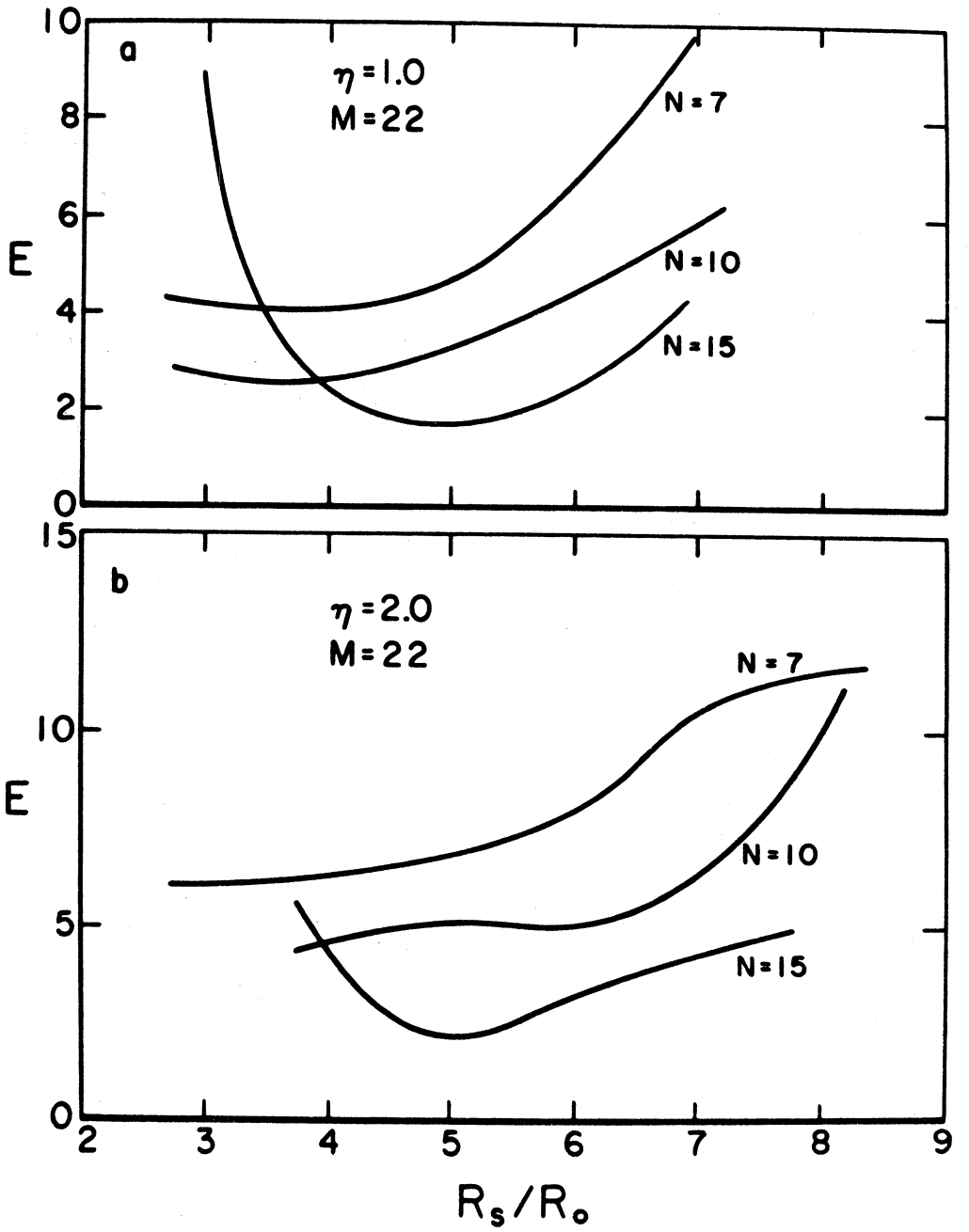

FIGURE 7 Error in Matching of Boundary Conditions as a Function of Source Locations -- Incident P-Waves

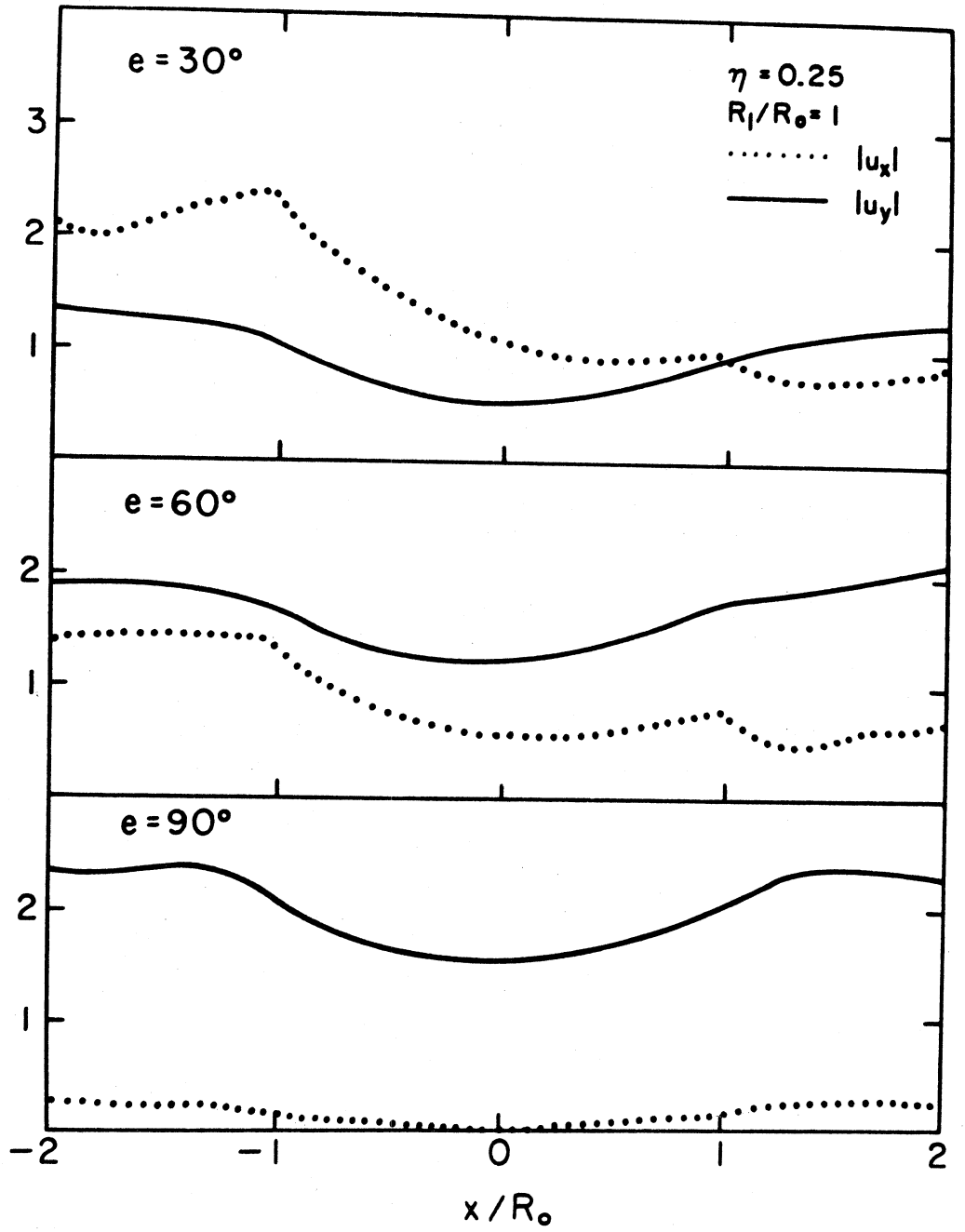

FIGURE 8 Amplification Patterns Induced by Incident P-Waves

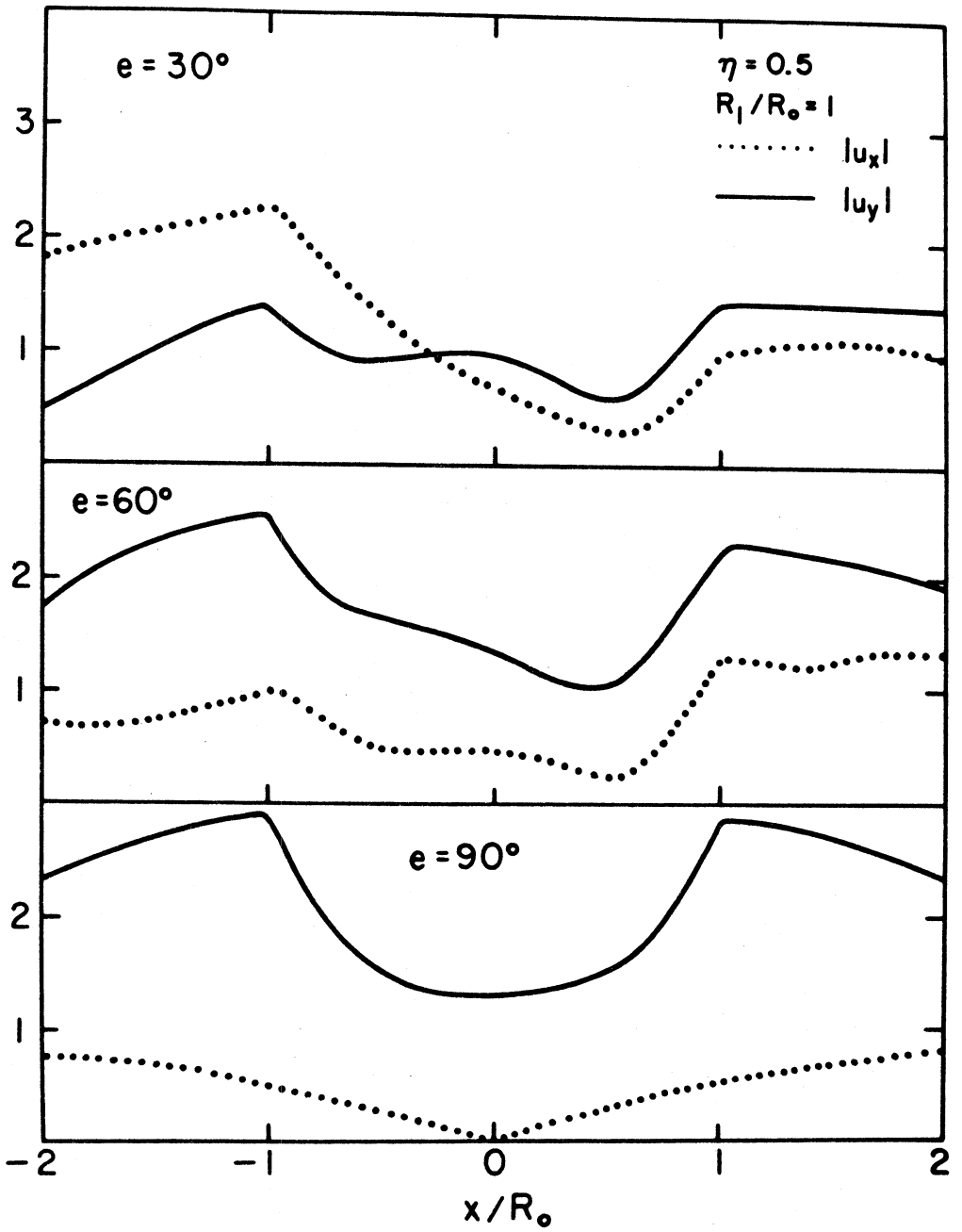

FIGURE 9 Amplification Patterns Induced by Incident P-Waves

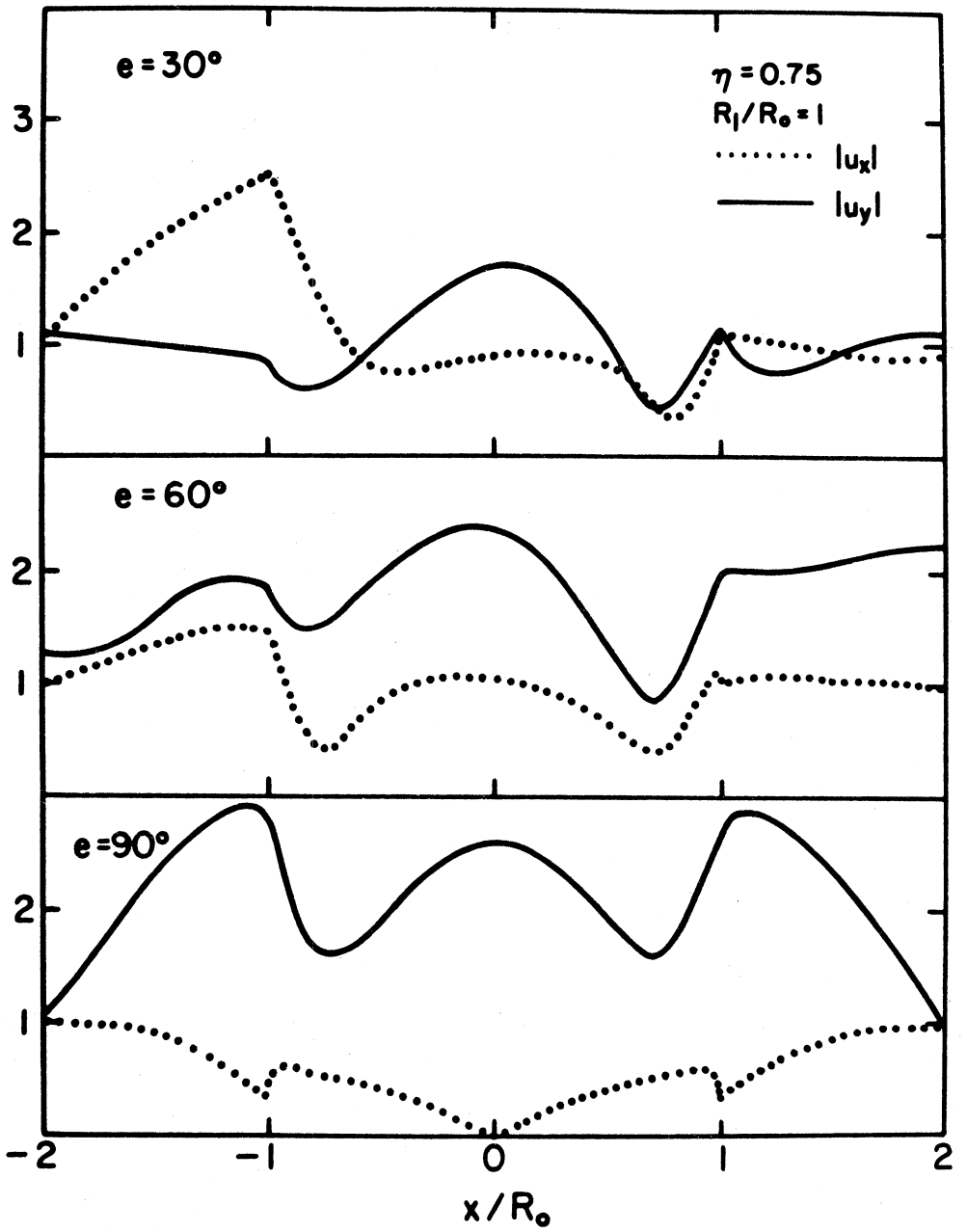

FIGURE 10 Amplification Patterns Induced by Incident P-Waves

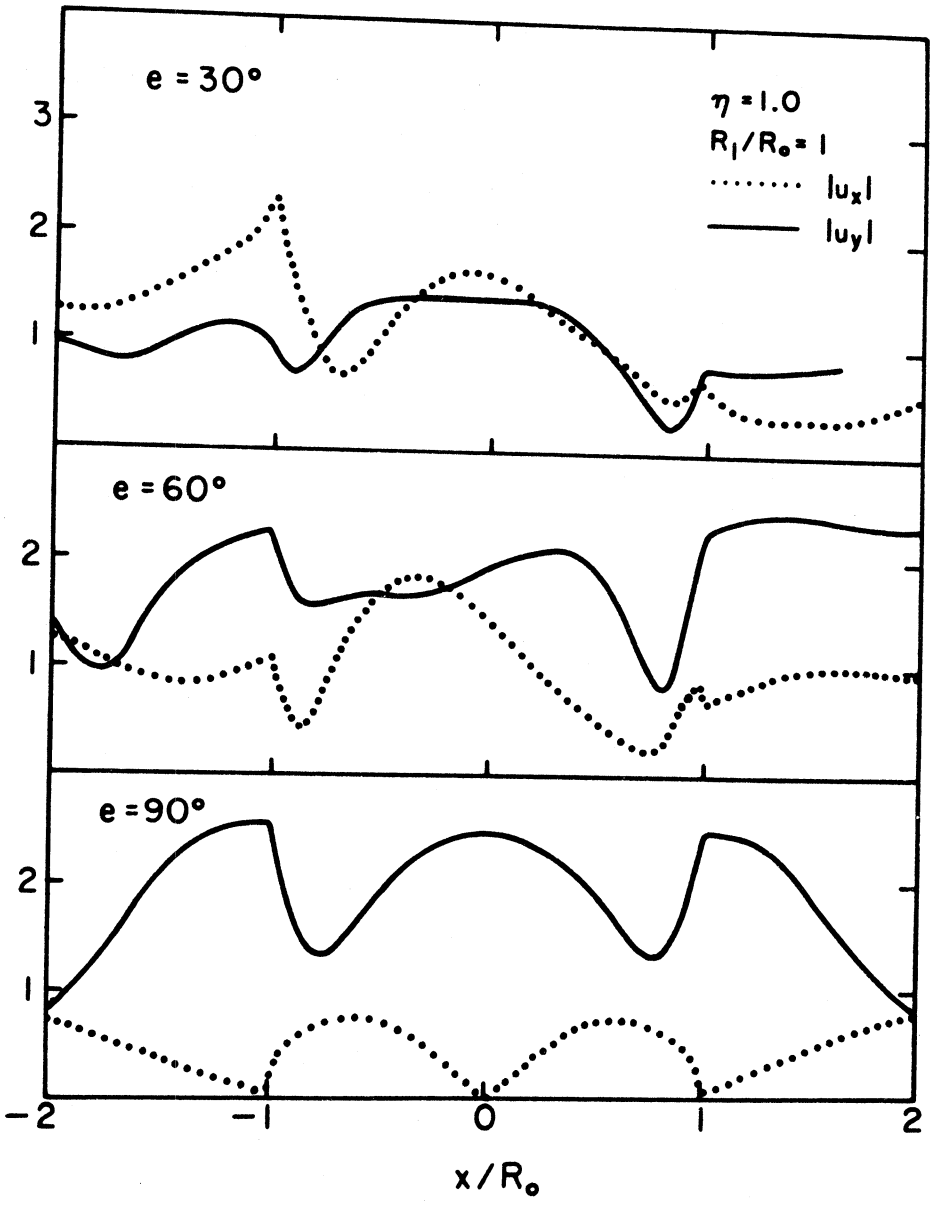

FIGURE 11 Amplification Patterns Induced by Incident P-Waves

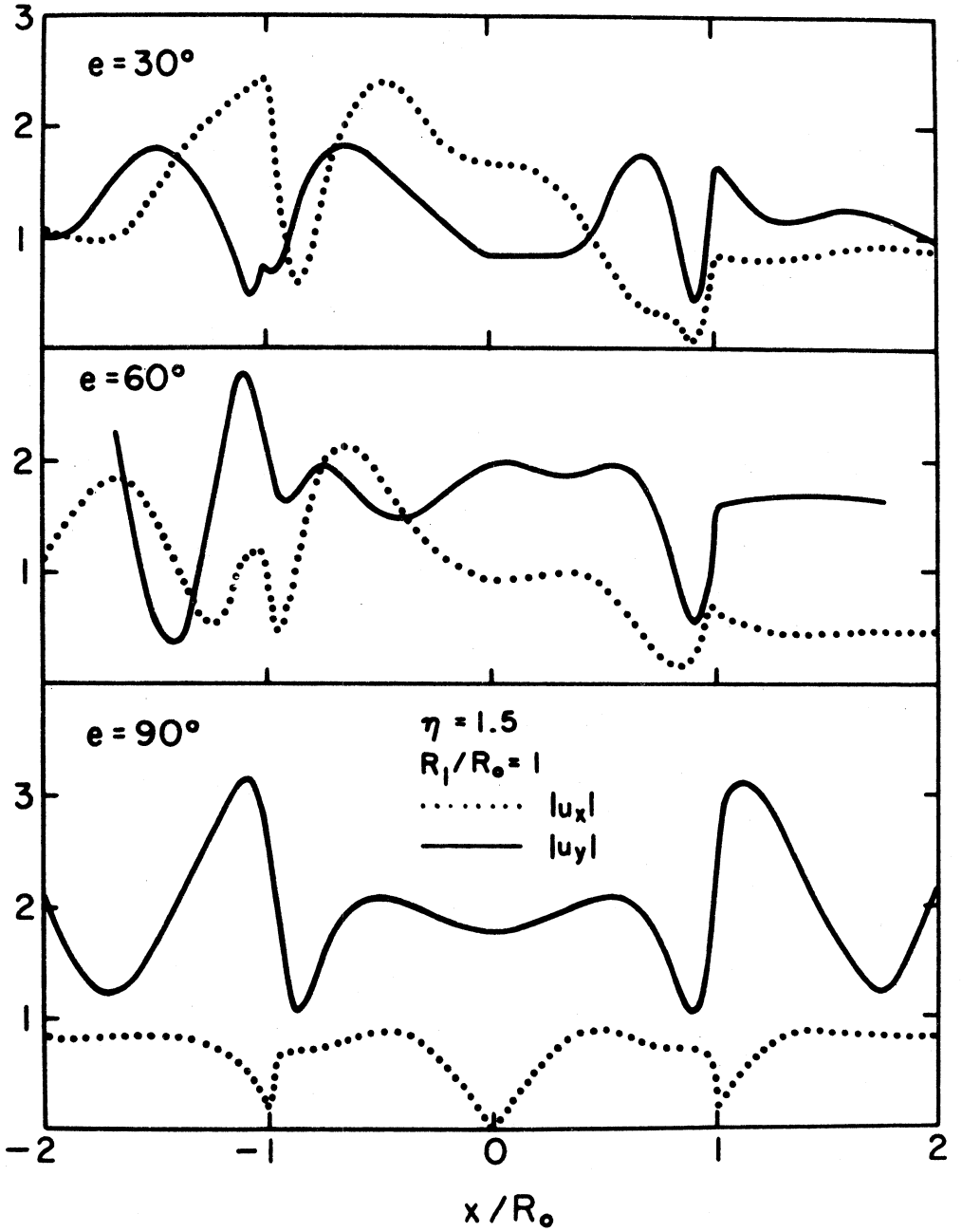

FIGURE 12 Amplification Patterns Induced by Incident P-Waves

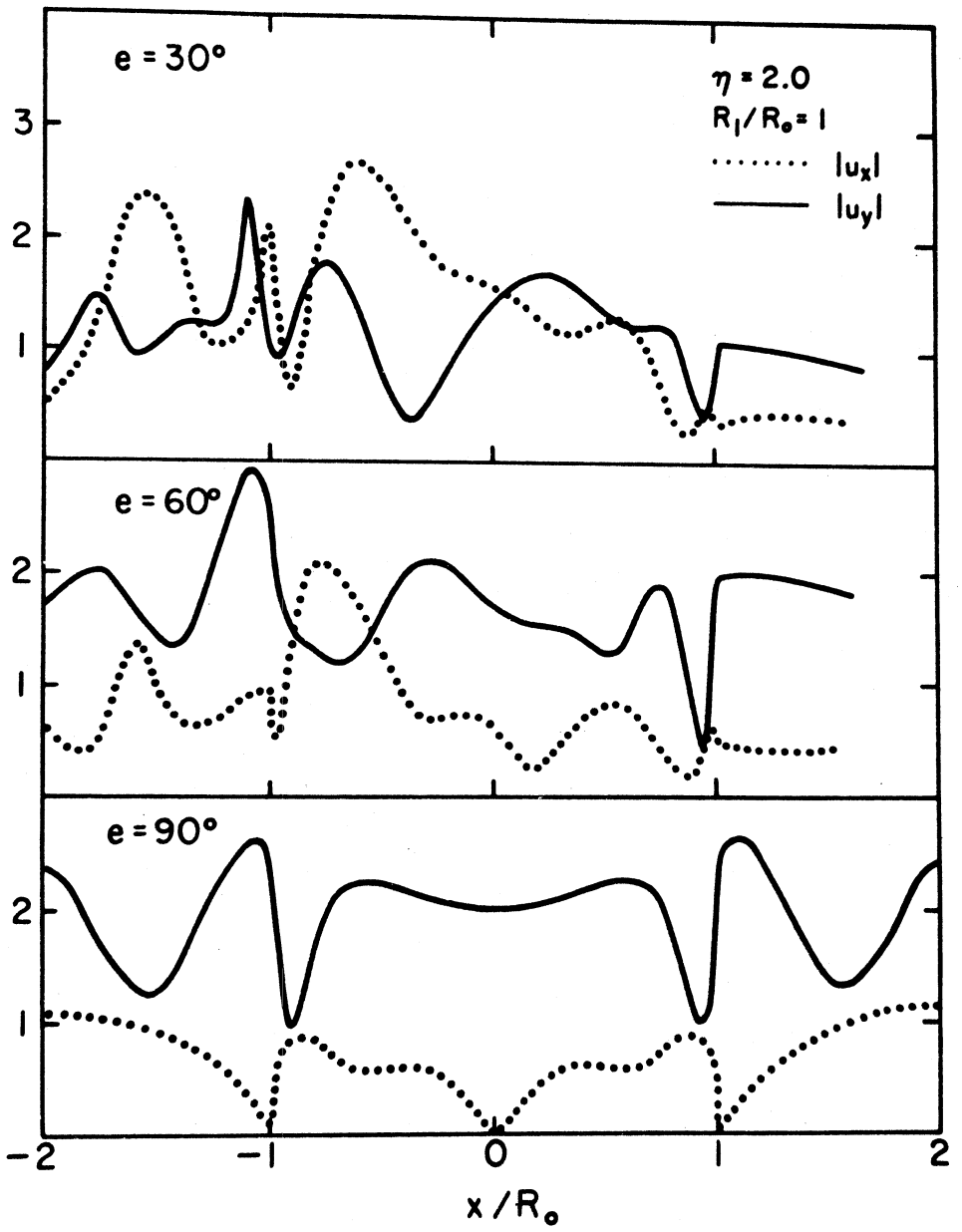

FIGURE 13 Amplification Patterns Induced by Incident P-Waves

A similar conclusion has been made in the SH case (Trifunac, 1973). There are large differences, however, between P and SH wave scattering, a phenomenon caused mainly by mode conversions in the former. For SH wave incidence, there are always some shielding effects behind the canyon, and the shielding improves as the frequency increases. For P wave incidence, however, either the vertical or horizontal component may be larger than the free field amplitudes. For example, the vertical component for e = 30° is larger than the free field value of 1.12 at η = 0.5 and 1.5; moreover, with $\eta < 1$, the vertical components for e = 60° is larger than the free field value of 1.74.

One particularly noticable difference between P and SH wave incidence is that the amplitudes at the rear of the shield can be larger than that at the front for a P wave. This reverse trend of amplification can be explained by the fact that some of the horizontal energy has been converted to vertical energy, or vice versa, through the stretching and compressing of the canyon surface.

The amplification of SV waves around a circular canyon shows further that a canyon or a trench does not necessarily shield away seismic waves. To demonstrate such effects, the diffraction patterns for $\eta = 0.5$, 1.0, 1.5 and 2.0 are shown in Figures 14 through 17; three angles of incidence, f = 60°, 75° and 90° are used for each dimensionless frequency. The angles less than the critical angle of 60 were not considered because the free field action becomes complex and attenuative in the y direction.

Once again, the amplification of SV waves by a circular canyon is less than 2 times that of the free field, a conclusion that should be identified

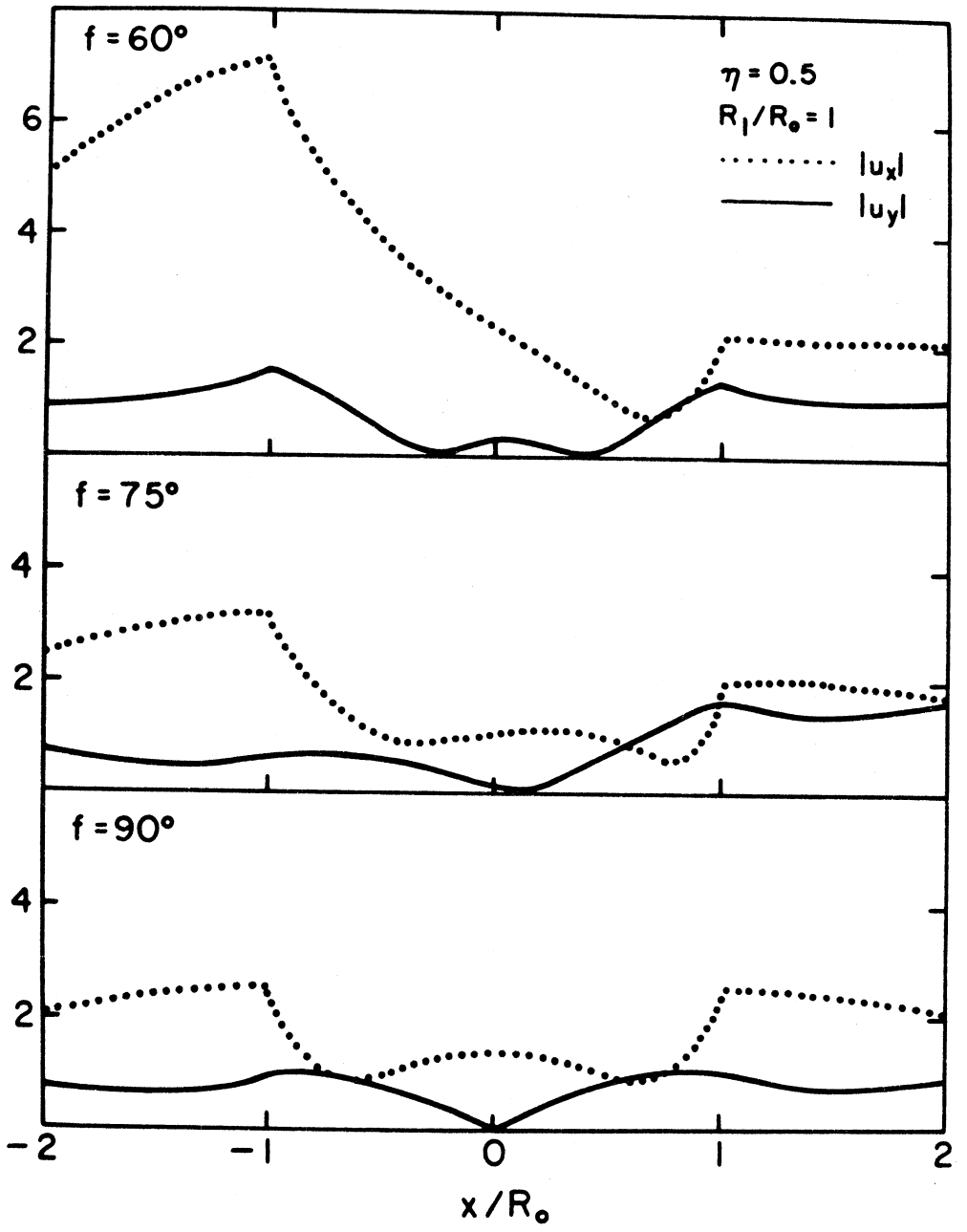

FIGURE 14 Amplification Patterns Induced by Incident SV-Waves

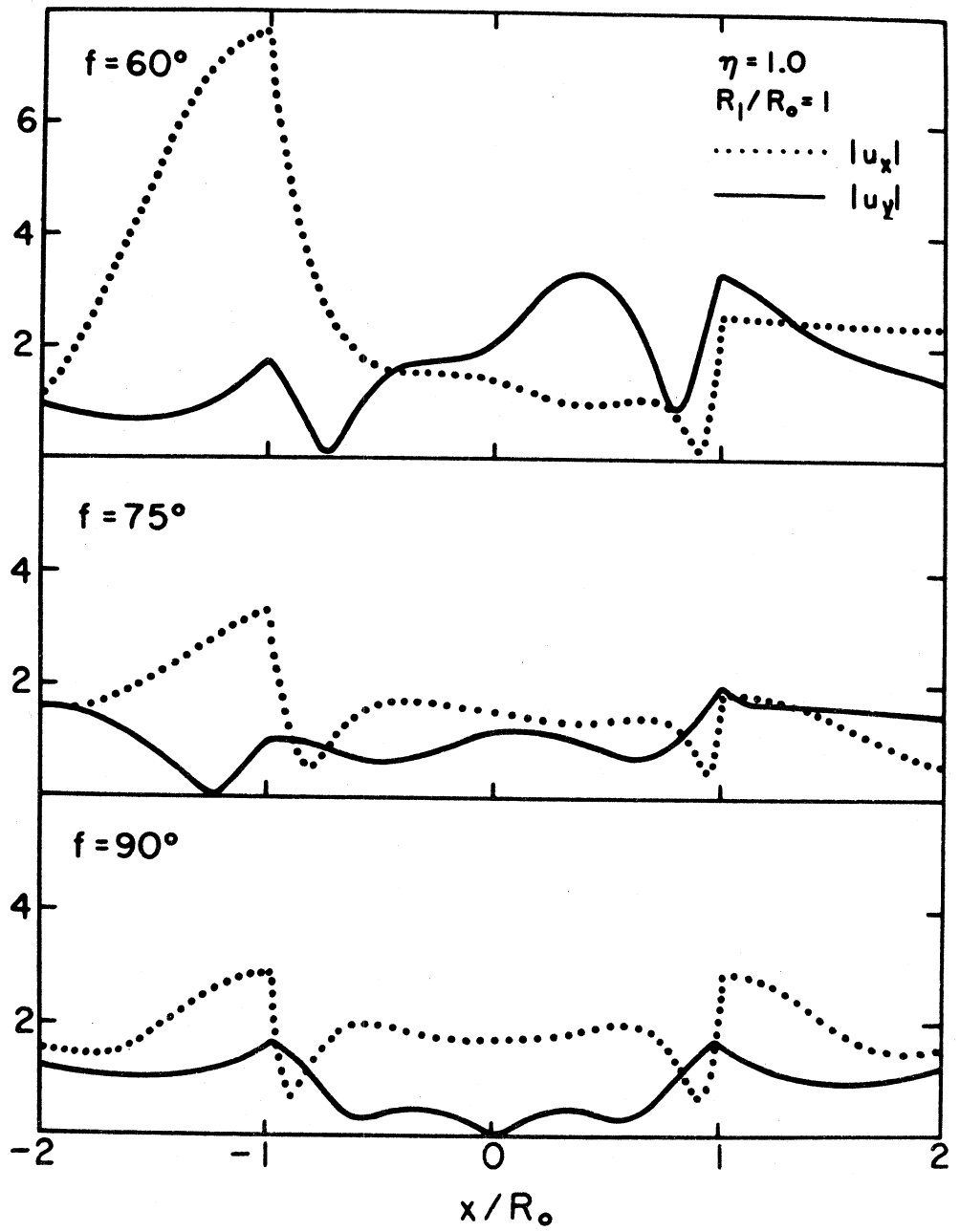

FIGURE 15 Amplification Patterns Induced by Incident SV-Waves

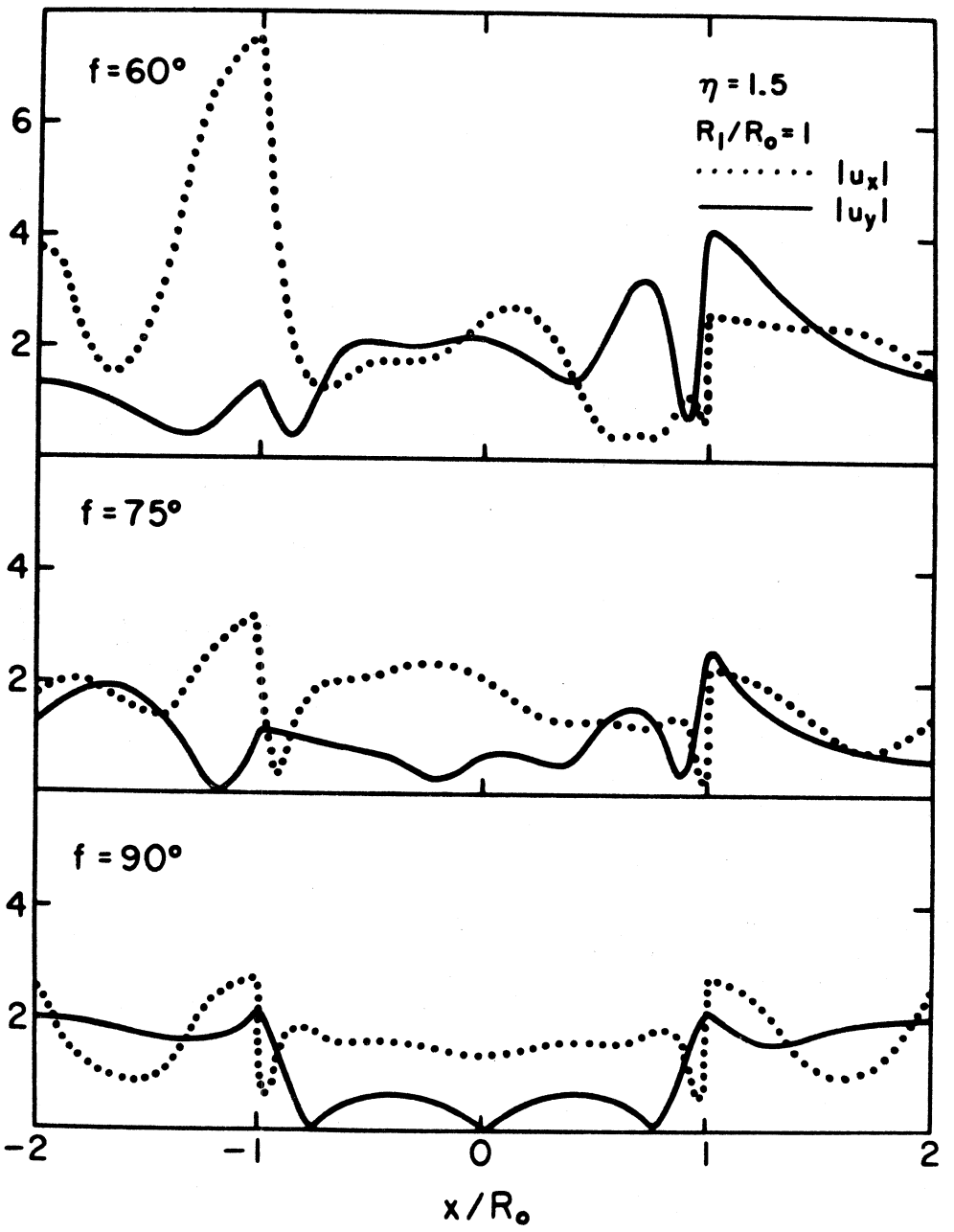

FIGURE 16 Amplification Patterns Induced by Incident SV-Waves

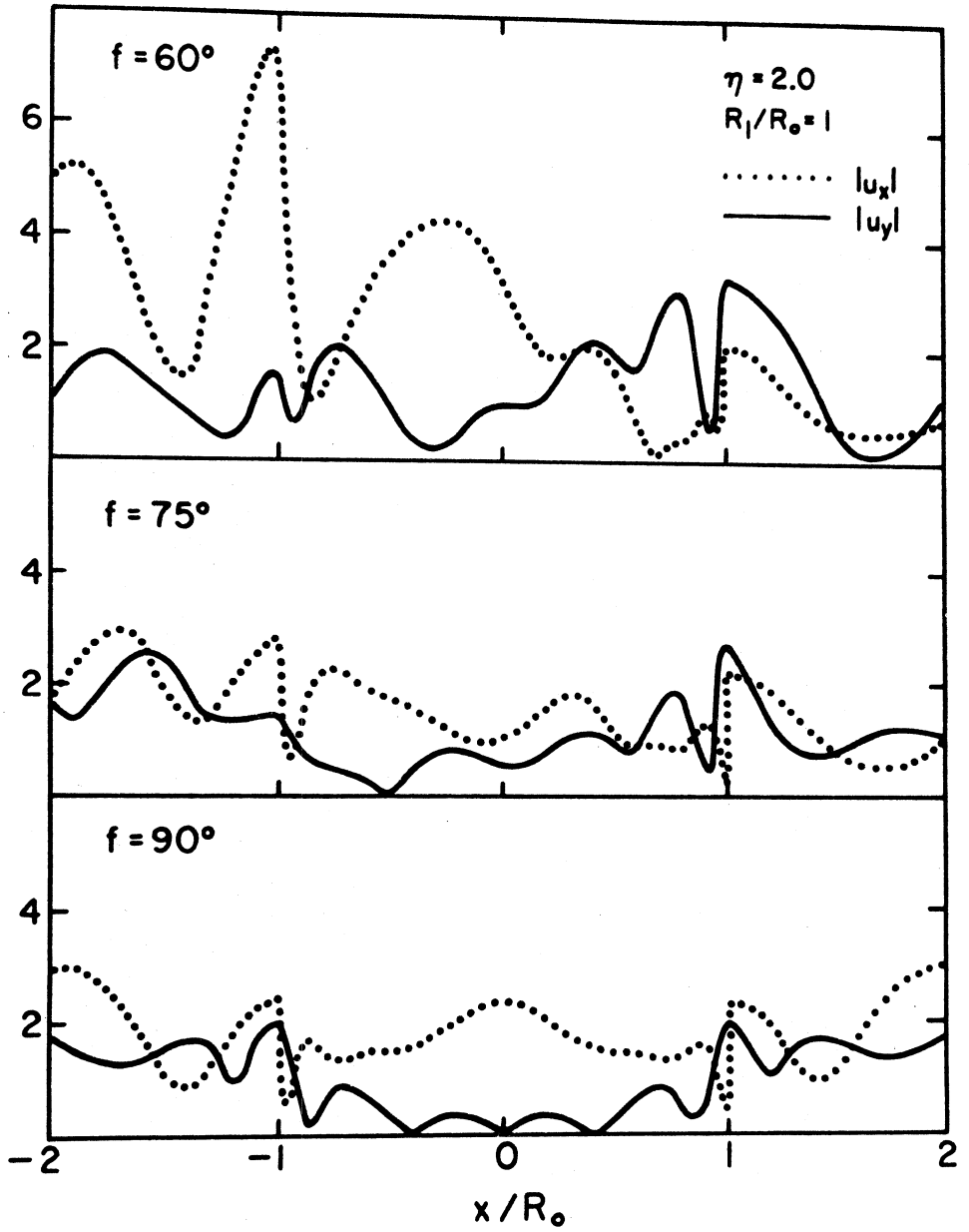

FIGURE 17 Amplification Patterns Induced by Incident SV-Waves

with the geometry of the scatterer rather than the wave type. The same type of mode conversion phenomena can be seen in the scattering of SV waves as in the P waves; however, the effects appear more prominent than those of P waves because the wavelength of SV waves is half that of P waves at the same frequency for a Poisson ratio of 1/3. Therefore, the presence of the canyon can be felt more readily by the waves and the diffraction patterns become more complicated. As a basis for comparison, the free field amplitudes for SV wave incidence in a half space are as follows

$$|u_x^{ff}| = 3.46 \quad , \quad |u_y^{ff}| = 0.00 \quad , \quad \text{for } f = 60° \ ,$$

$$|u_x^{ff}| = 1.94 \quad , \quad |u_y^{ff}| = 0.50 \quad , \quad \text{for } f = 75° \ ,$$

$$|u_x^{ff}| = 2.00 \quad , \quad |u_y^{ff}| = 0.00 \quad , \quad \text{for } f = 90° \ .$$

It is interesting to note that the free field vertical components are zero for $f = 60°$ and $f = 90°$; thus, any nonzero vertical responses around the canyon are induced purely by scattering from the canyon. With $f = 60°$ and for all frequencies, the vertical component increases gradually from the front of the canyon toward the rear as some of the horizontal energy is converted to vertical energy. It is important to consider the fact that the amplitude of $|u_y|$ can be as large as 4 at some locations behind the canyon ($x/R_o > 1$) and these amplitudes are caused strictly by mode conversions. Therefore, with only a minimal amount of shielding provided by the canyon for the horizontal component, it cannot compensate for the large amplification of the vertical component.

Other considerations for the wave diffraction pattern is that

standing waves form only in front of the canyon, where the constructive and destructive interferences of the incidence and reflected waves occur. While the translational components are diminished by the cancelling effect at the points of destructive interferences, a large rotational component generally occurs because the derivative of a harmonic function is maximum when the value is minimum. The rotations that are associated with the vertical component (P or SV waves) are of the rocking type while the rotation associated with the SH waves are of the torsion type. Both these rotational components have a strong effect on the structural responses during an earthquake. The quiet points for the horizontal component of P or SV waves represent true quiet points, but since the location of these points are frequency dependent, they have no practical values.

To account for the geometrical effect of the canyon, the depth of the canyon is reduced to a ratio $R_1/R_o = 0.5$ for the next analyses. The results for $|u_x|$ and $|u_y|$ are represented for incidence P wave in Figures 18 through 21. The overall differences from the free field amplitudes are reduced because the size of the topography has been reduced. The diffraction pattern and the mode conversion effects, however, are very similar to those of the circular canyon.

Numerically, the calculation of amplitudes for $|x/R_o > 1|$ is more difficult for shallow canyons than for deep canyons because there is less volume at which the singular sources can be placed. As the result, the sources are bunched closer together within the boundary of a shallow canyon, causing the matrix equation to be ill-conditioned to various

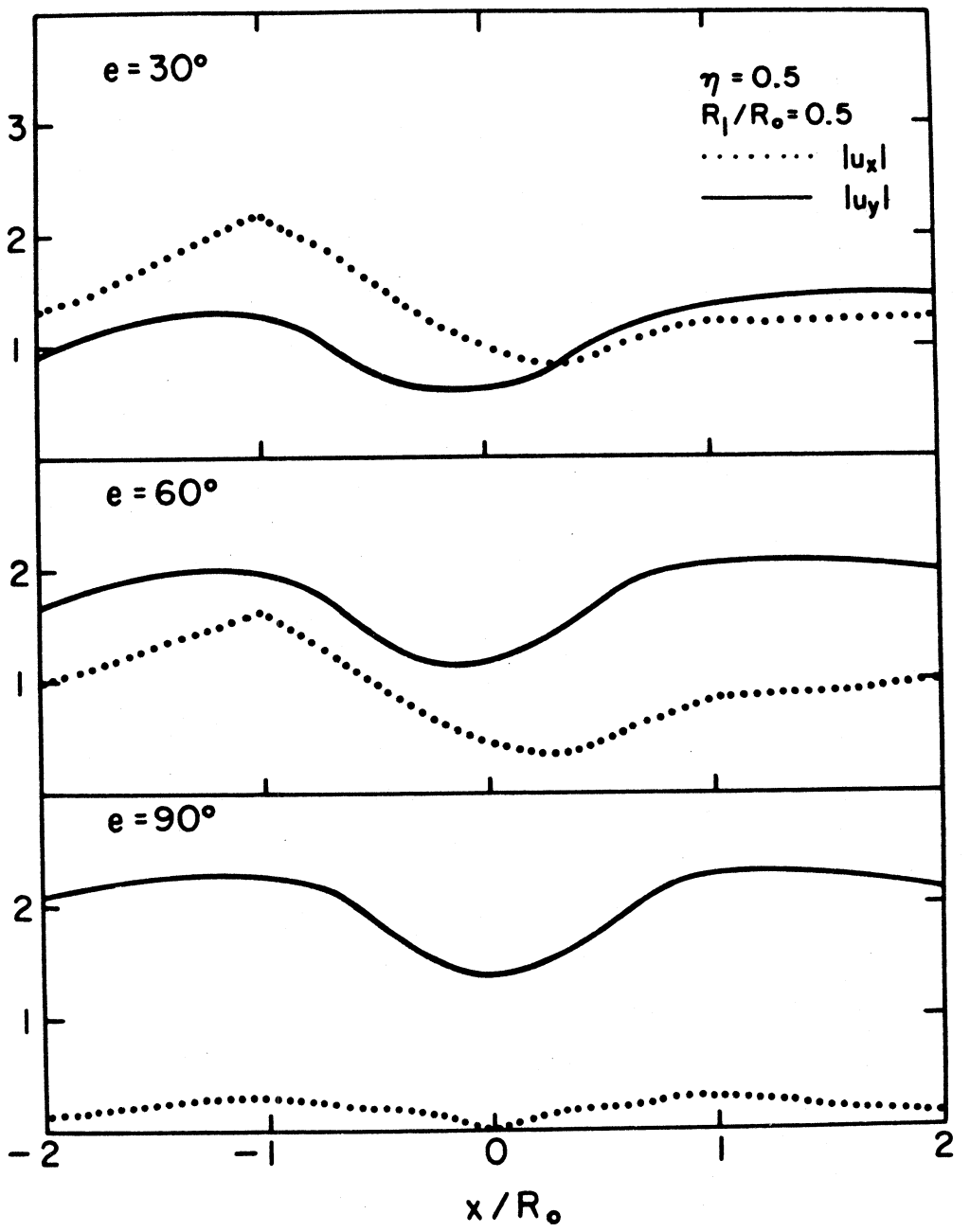

FIGURE 18 Amplification Patterns Induced by Incident P-Waves

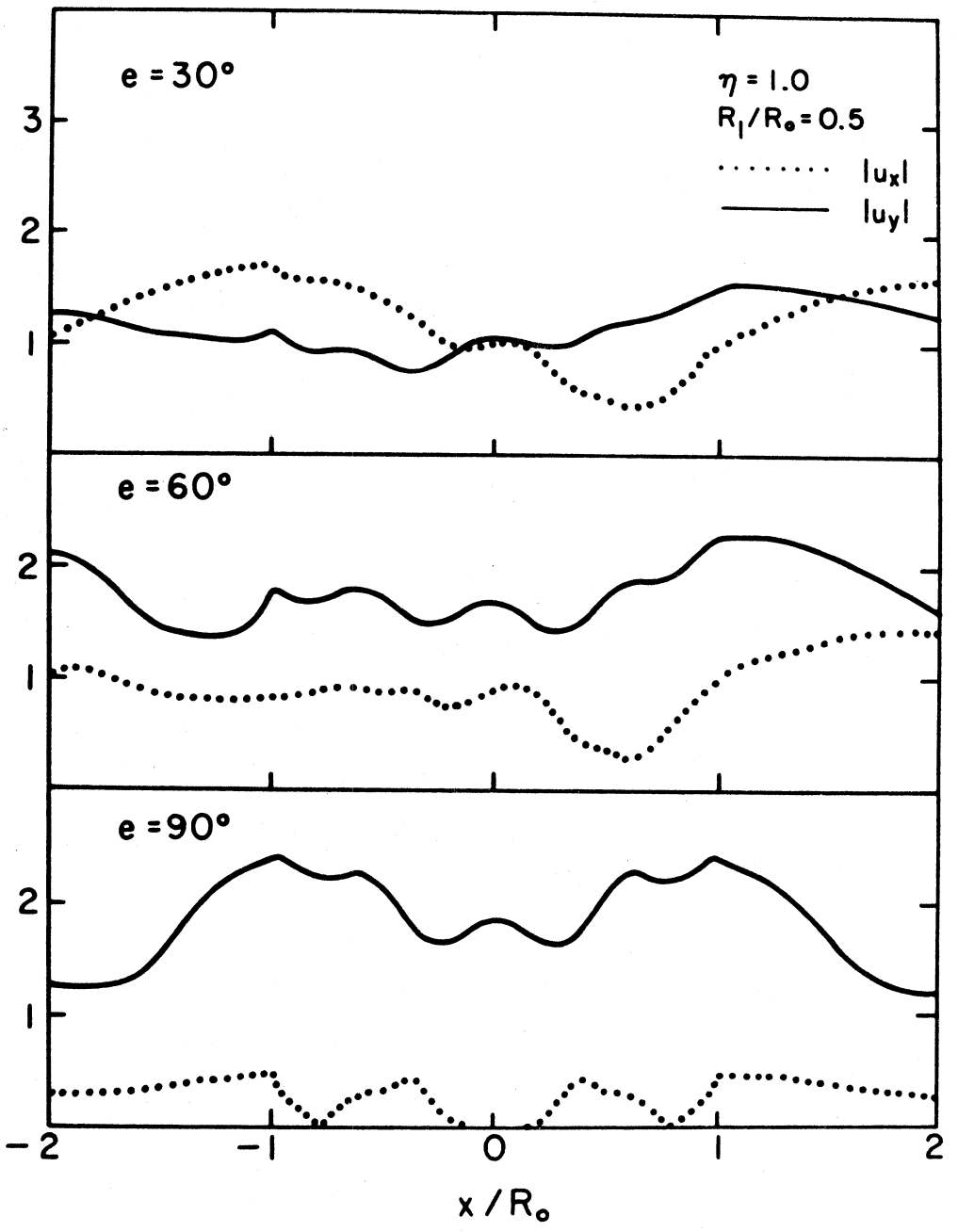

FIGURE 19 Amplification Patterns Induced by Incident P-Waves

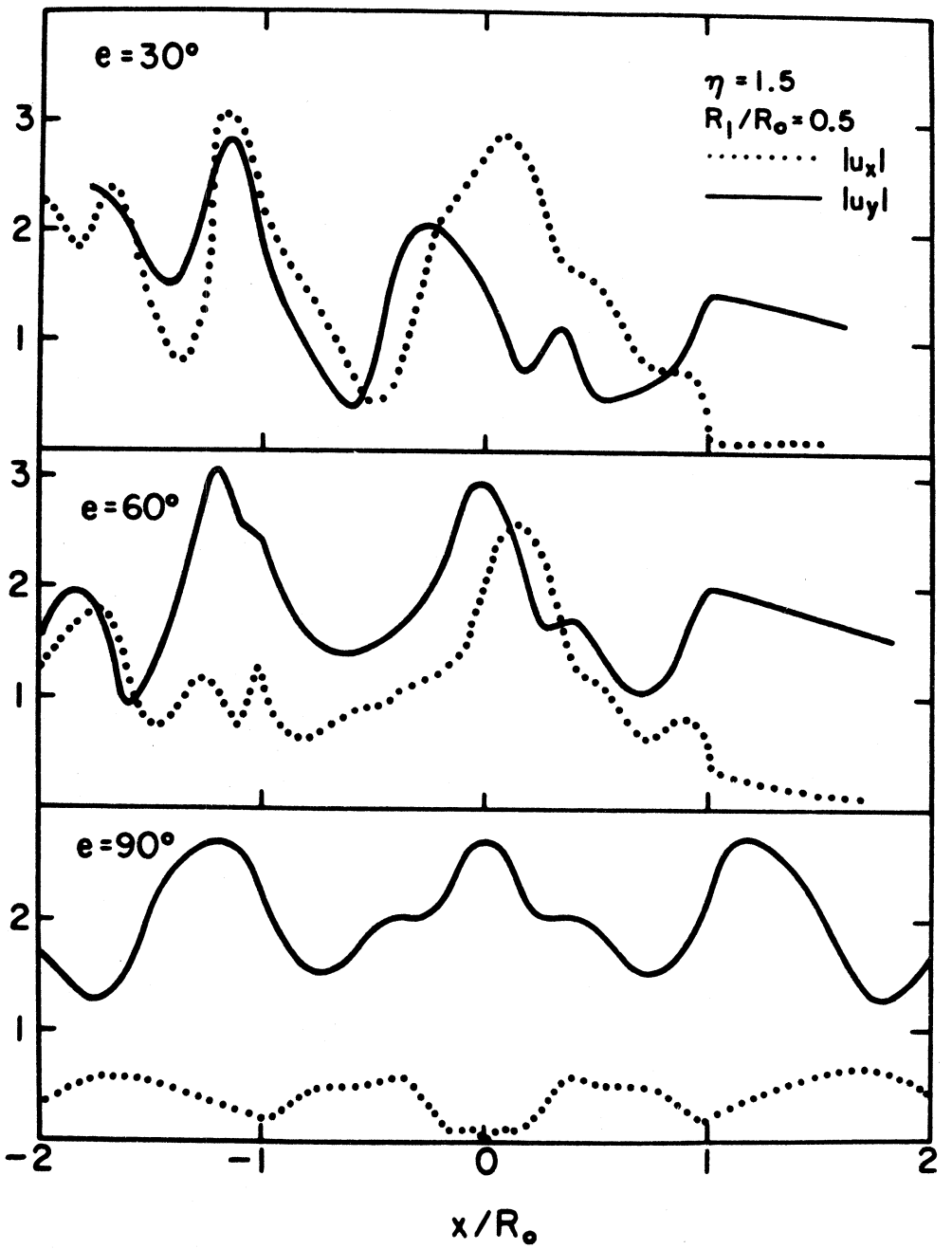

FIGURE 20 Amplification Patterns Induced by Incident P-Waves

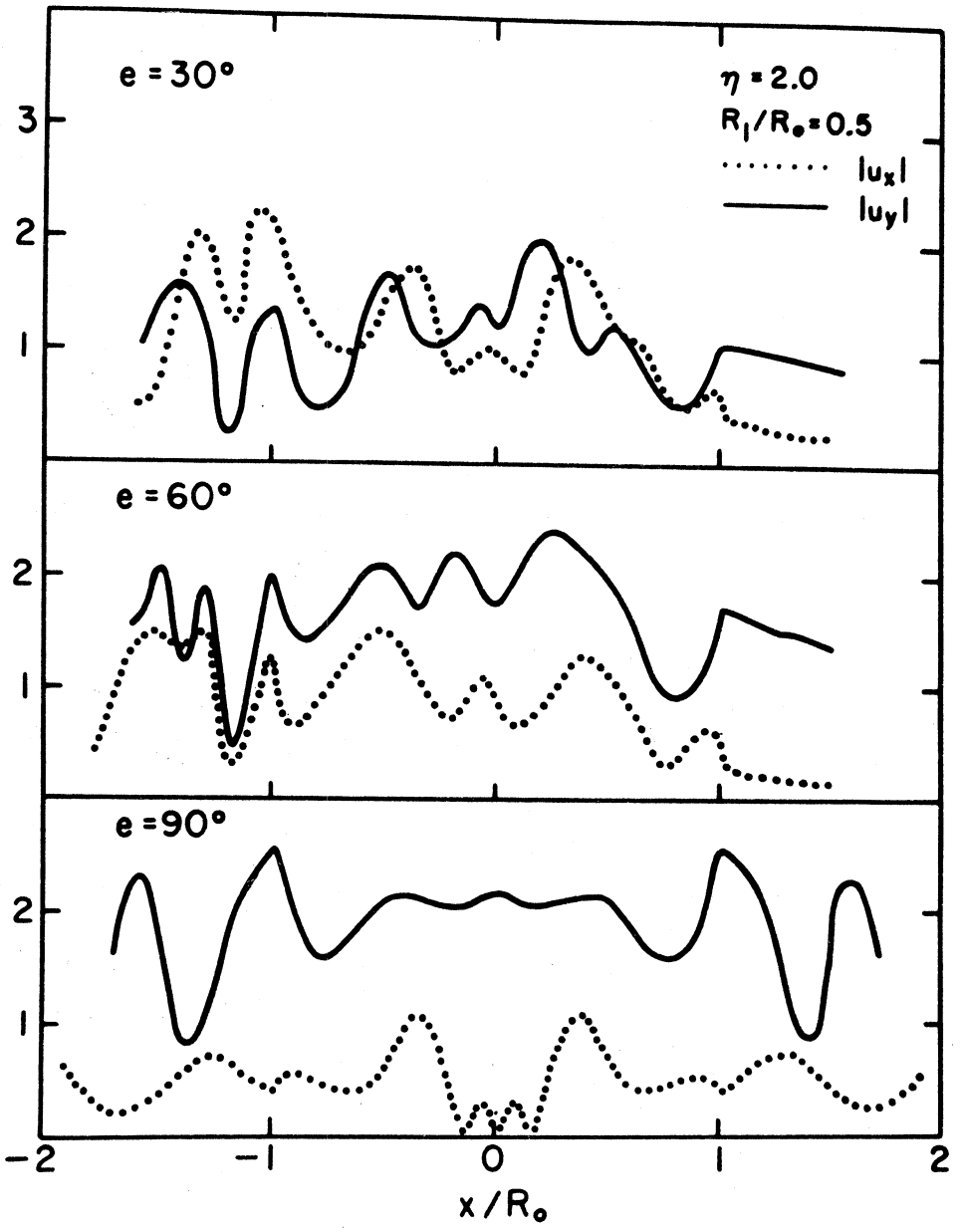

FIGURE 21 Amplification Patterns Induced by Incident P-Waves

degrees depending on the frequency. Thus, the only way to improve the numerical solution for shallow boundaries is to significantly improve the accuracy of the line source solutions. At present, the line source solutions of Appendix B can be calculated with an accuracy of 4 digits; further improvement would require a laborious computational effort.

Diffraction of Rayleigh Waves by a Circular Canyon

In two-dimensional plane strain wave propagation problems, the Rayleigh surface wave tends to be more influential than the P or SV waves. Due to the lower frequency content and the retrograde type motion, the Rayleigh waves have been considered to be the main cause for many observed damages. In fact, as explained by Cherry (1973), the retrograde motion is most effective in causing landslides in unstable slopes.

In this section, the diffraction of a Rayleigh wave by a circular canyon will be examined. Since the Rayleigh waves attenuate exponentially in depth and it is only "skin" deep at high frequencies, the shielding property of a canyon is entirely different from that of P or SV wave incidence.

Although the wave type is different, the method of numerical calculation is the same as that of the previous section; only the expressions of the free field motion need to be changed. The free field displacements and stresses generated by a Rayleigh wave are compiled in Appendix D. They can be readily substituted into equations (48) through (52) for the present analysis. The wave amplification patterns of $|u_x|$ and $|u_y|$ generated by a Rayleigh wave propagating from left to right is shown in Figure 22 for η = 0.5, 1.0, 1.5 and 2.0. Except for η = 0.50, a low frequency case, the reduction of wave amplitudes at the rear of the canyon is significant. With a free field amplitude of $|u_x|$ = 1.0 and $|u_y|$ = 1.56 for a Poisson ratio of 1/3, the reduction of amplitude is approximately

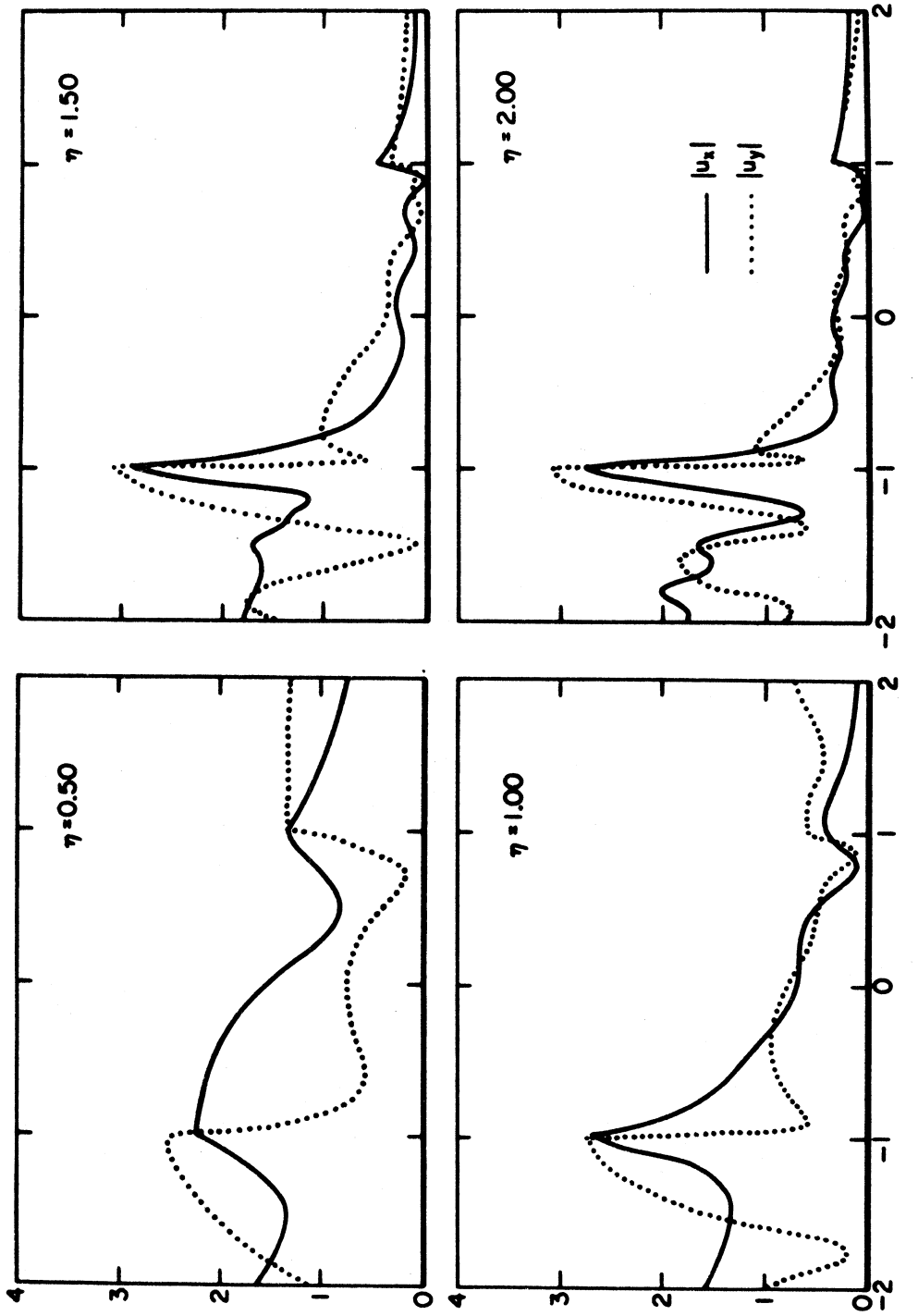

FIGURE 22 Amplification Patterns Induced by Incident Rayleigh Waves

80% for $\eta > 1.25$,

50% for $0.75 < \eta < 1.25$,

and uncertain for $\eta < 0.75$;

thus, an effective shield can be provided for high frequency Rayleigh waves.

It is important to point out that the amplitude of waves is nearly doubled at the front edge of the canyon ($x/R_o = -1$) and the phase of the two components differs by approximately $\pi/2$, indicating that a retrograde motion is retained. These complicated motions can be understood more readily by viewing a series of time elapsed figures of the deformation shown in Figure 23 for $\eta = 0.5$, 1.0, 1.5 and 2.0. If all 8 frames are placed one over another, the motion of the corner $x/R_o = -1$ will map out a titled ellipse with a ratio different from that of the free field motion.

Perhaps the most interesting phenomenon is displayed in frames

$t = \frac{5}{4}\pi$ for $\eta = 0.5$,

$t = \frac{3}{4}\pi$ for $\eta = 1.0$,

$t = 0$ for $\eta = 1.5$,

$t = \frac{7}{4}\pi$ for $\eta = 2.0$,

all of which indicate materials being thrown out into the canyon, a process that may cause landslides of the slopes. Although the deformations in Figure 23 are greatly exaggerated and the slope of the circular canyon is larger than most realistic embankments, this analysis shows nevertheless the possible effect of a Rayleigh incident wave.

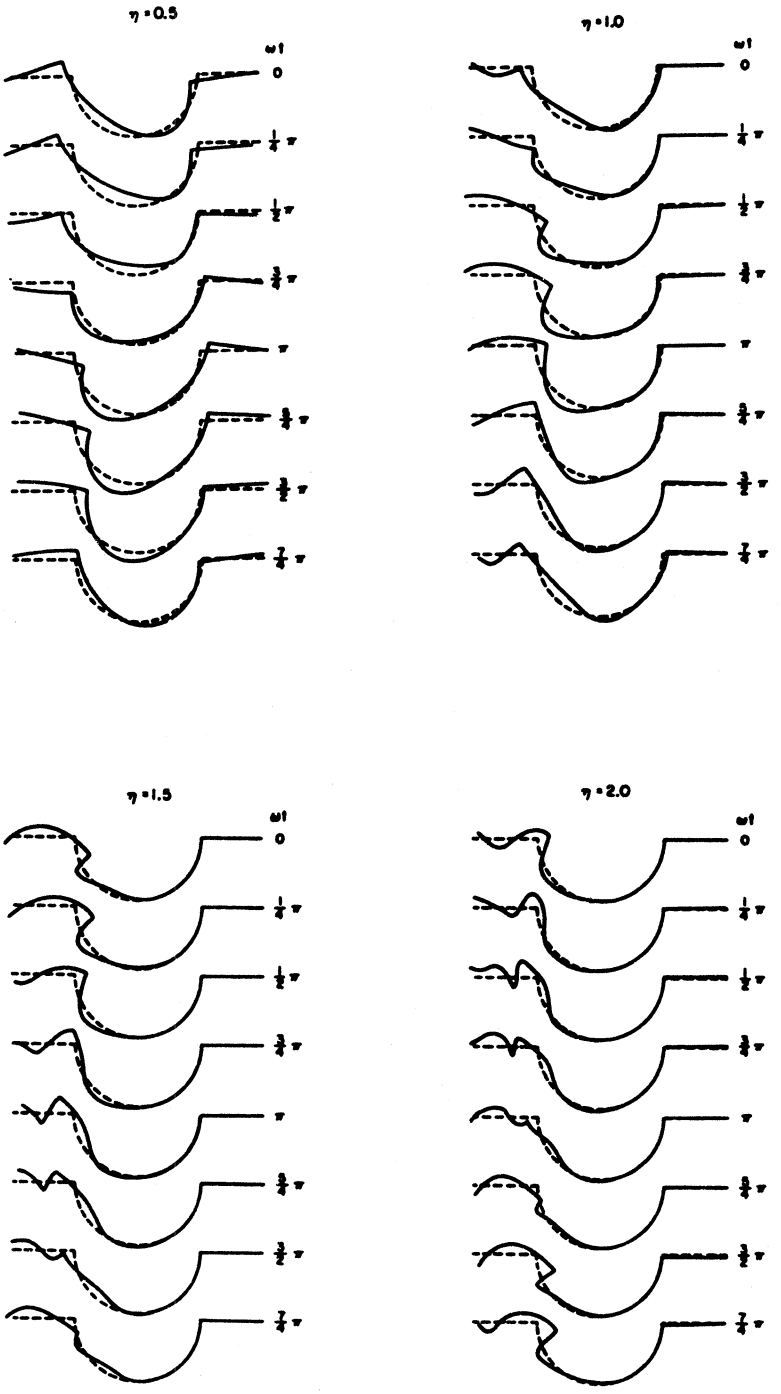

FIGURE 23 Time Elapsed Motions of a Canyon Excited by a Harmonic Rayleigh Wave

Conclusions

The method of Ohsaki has been adapted for elastic wave propagation problems. Through the comparison with two exact solutions of different nature, the approximate method has been shown to have adequate accuracy for most applications. This method is most effectively applied to problems where most of the boundary conditions can be satisfied by the basis of the solution, leaving just one or two difficult boundary conditions for the generalized inverse procedure.

As an important application of this numerical method, the scattering of P, SV or Rayleigh waves by an elliptical canyon was analyzed. The results can be summarized as follows:

(i) The amplitude of waves near an elliptical canyon is less than 2 times the free field amplitudes. The fact of 2 is associated with the canyon geometry rather than the wave types.

(ii) For P or SV wave incidence, the large amplification does not always occur in front of the canyon; the idea of applying a shield to an important structure may not be valid.

(iii) Standing wave phenomena caused by interference of wave occur only in front of the canyon. Large amplitudes at the rear of the canyon are caused by mode conversions.

(iv) Rayleigh waves with wavelength shorter than the width of the canyon can be blocked effectively by the canyon, but the front edge of the shield may suffer slope instabilities due to the retrograde motion induced by a Rayleigh wave.

References

Aki, K., and K.L. Larner (1970). Surface motion of a layered medium having an irregular interface due to incident plane SH-waves, J. Geophysical Res., Vol. 75, 933-954.

Alterman, Z., and F.C. Karal (1968). Propagation of elastic waves in layered media by finite difference methods, Bull. Seism. Soc. Am., Vol. 63, 615-632.

Asano, S. (1966). Reflection and refraction of elastic waves at a corrugated surface, Bull. Seism. Soc. Amer., Vol. 50, 201-222.

Banaugh, R. P., and W. Goldsmith (1963). Diffraction of steady acoustic waves by surfaces of arbitrary shape, Journal of Acoust. Soc. of Amer., Vol. 35, No. 10, 1590.

Bouchon, M. (1973). Effect of topography on surface motions, Bull. Seism. Soc. Amer., Vol. 63, 615-632.

Boore, D.M. (1972a). Finite difference method for seismic wave propagation in hererogeneous materials, Methods in Computational Physics, Vol. II, editor, B.A. Bolt, Academic Press.

Boore, D.M. (1972b). A note on the effect of simple topography on seismic SH-waves, Bull. Seism. Soc. Amer., Vol. 62, 275-284.

Bradford, L.G., S.B. Dong, D.A.C. Nicol, and R.A. Westman (1976). Application of global-local finite element method to fracture mechanics, Electric Power Research Institute Report EPRI NP-239.

Cherry, J.T. (1973). Calculation of near field, earthquake ground motion, System, Science and Software, Technical Report SSS-R-73-1759, La Jolla, California.

Chopra, A.K. (1969). Earthquake analysis of earth dams, Proc. 4th World Conf. Earthquake Eng., Vol. 3, A5:55-72, Santiago, Chile.

Chopra, A.K., P. Chakrabarti, and G. Dasgupta (1975). Frequency dependent stiffness matrix for viscoelastic half space foundations, EERC Report 75-22, U.C. Berkeley, California.

England, R., F.J. Sabina, and I. Herrera (1978). Scattering of SH waves by superficial cavities of arbitrary shape using boundary methods, Vol. 9, 1978 Serie Naranja: Investigaciones, #180, Universidad Nacional Autonoma de Mexico.

Fung, Y.C. (1965). Foundation of solid mechanics, Prentice-Hall, Englewood Cliffs, New Jersey.

Jennings, P.C. (Editor) (1971). San Fernando Earthquake of February 9, 1971, EERL 71-02, California Institute of Technology, Pasadena, California.

Lamb, H. (1904). On the propagation of tremors over the surface of elastic solid, Phil. Trans. Royal Soc. (London) A, Vol. 203, pp. 1-42.

Larner, K.L. (1970). Near-receiver scattering of teleseismic body waves in layered crust-mantle models having irregular interfaces, Ph.D. Thesis, M.I.T., Cambridge, MA.

McIvor, I. (1969). Two-dimensional scattering of a plane compressional wave by surface imperfection, Bull. Seism. Soc. Amer., Vol. 59, 1359-1364.

Mow, C.C., and Y.H. Pao (1973). The diffraction of elastic waves and stress concentrations, RAND Report R-482-PR.

Noble, B. (1969). Applied Linear Algebra, McGraw Hill, New Jersey.

Ohsaki, Y. (1973). On movements of a rigid body in semi-infinite elastic medium, Proc. of the Japanese Earthquake Engng. Symp., Tokyo, Japan.

Reimer, R.B., R.W. Clough and J.M. Raphael (1974). Seismic response of Pacoima Dam in San Fernando Earthquake, Proc. 5th World Conf. Earthquake Engng., Vol. 2, 2328-2337, Rome, Italy.

Sabina, F.J., and J.R. Willis (1975). Scattering of SH-waves by a rough half space of arbitrary shape, Geophysical Journal, Vol. 42, 685-703.

Sanchez-Sesma, F.J., and E. Rosenblueth (1978). Movimiento del terreno en cepresiones bidimensionales de forma aribitraria ante incidencia de ondes SH planas, in Evaluacion del riesgo-efectos locales, etana I, Institutu de Ingenieria, U.N.A.M., Mexico, Ingenieria Sismica, Mexico.

Smith, W.D. (1974). The application of finite element analysis to body wave propagation problems, Tenth Int. Symp. Math. Geophysics, Cambridge, Massachussetts.

Smith, W.D. (1977). The application of finite element analysis to body wave propagation problems, Geophysical J. Royal Ast. Soc.,

Sozen, M.A., P.C. Jennings, R.B. Mathiesen, G.W. Housner, and N.M. Newmark (1968). Engineering report on the Caracas earthquake of 29 July, 1967, National Academy of Sciences, Washington, D.C.

Trifunac, M.D. (1973). Scattering of plane SH-waves by a semi-cylindrical canyon, Earthquake Engng. Struct. Dyn., Vol. 1, 267-281.

Trifunac, M.D. (1971). Surface motion of a semi-cylindrical alluvial valley for incident plane SH waves, Bull. Seism. Soc. Am., 61, 1755-1770.

Wong, H.L., and M.D. Trifunac (1974a). Scattering of plane SH-wave by a semi-elliptical canyon, Earthquake Engng. Struct. Dyn., Vol. 3, 157-169.

Wong, H.L., and M.D. Trifunac (1974b). Surface motion of a semi-elliptical alluvial valley for incident plane SH-waves, Bull. Seism. Soc. Amer., Vol. 64, 1389-1408.

Wong, H.L., and P.C. Jennings (1975). Effect of canyon topographies on strong ground motion, Bull. Seism. Soc. Am., Vol. 65, 1239-1257.

Wong, H.L., M.D. Trifunac, and B.D. Westermo (1977). Effect of surface and subsurface irregularities on the amplitude of monochromatic waves, Bull. Seism. Soc. Am., Vol. 67, 353-368.

Zienkiewicz, O.C. (1977). The Finite Element Method, Chapter 23, 3rd Edition, McGraw Hill Book Company (U.K.).

Zienkiewicz, O.C., D.W. Kelly, and P. Bettess (1977). The coupling of the finite element method and boundary solution procedures, Int. J. Num. Meth. Eng., Vol. 11, 355-276.

ACKNOWLEDGEMENTS

The author expresses appreciation to Professor J.E. Luco for suggesting the method and to Dr. M. Dravinski for critical reading of the manuscript.

This research was supported by a grant from the United States Geological Survey.

APPENDIX A

Displacements and Stresses Generated by Line Sources in an Infinite Elastic Medium

(1) Compressional Wave Source at Point (x,y) = (0,0)

$$\hat{\phi}(x,y \mid 0,0) = H_o^{(2)}(hr) \tag{A.1}$$

$$\hat{u}_x^{\phi}(x,y \mid 0,0) = -\frac{hx}{r} H_1^{(2)}(hr) \tag{A.2}$$

$$\hat{u}_y^{\phi}(x,y \mid 0,0) = -\frac{hy}{r} H_1^{(2)}(hr) \tag{A.3}$$

$$\frac{1}{\mu}\hat{\sigma}_{xx}^{\phi}(x,y \mid 0,0) = -\frac{(1-2\gamma^2)}{\gamma^2} h^2 H_o^{(2)}(hr) + 2\left\{h\left[\frac{2x^2}{r^3} - \frac{1}{r}\right] H_1^{(2)}(hr) - \frac{h^2x^2}{r^2} H_o^{(2)}(hr)\right\} \tag{A.4}$$

$$\frac{1}{\mu}\hat{\sigma}_{yy}^{\phi}(x,y \mid 0,0) = -\frac{(1-2\gamma^2)}{\gamma^2} h^2 H_o^{(2)}(hr) + 2\left\{h\left[\frac{2y^2}{r^3} - \frac{1}{r}\right] H_1^{(2)}(hr) - \frac{h^2y^2}{r^2} H_o^{(2)}(hr)\right\} \tag{A.5}$$

$$\frac{1}{\mu}\hat{\sigma}_{xy}^{\phi}(x,y \mid 0,0) = 2xy\left\{\frac{2h}{r^3} H_1^{(2)}(hr) - \frac{h^2}{r^2} H_o^{(2)}(hr)\right\} \tag{A.6}$$

where

$$h = \frac{\omega}{\alpha}$$

$$\gamma = \frac{\beta}{\alpha}$$

$$r = \sqrt{x^2 + y^2}$$

α = compressional wave velocity,

β = shear wave velocity,

$H_o^{(2)}, H_1^{(2)}$ = Hankel's function of the second kind, zero and first order, respectively.

(2) Shear Wave Source at Point $(x,y) = (0,0)$

$$\hat{\psi}(x,y \mid 0,0) = H_o^{(2)}(kr) \tag{A.7}$$

$$\hat{u}_x^{\psi}(x,y \mid 0,0) = -\frac{ky}{r} H_1^{(2)}(kr) \tag{A.8}$$

$$\hat{u}_y^{\psi}(x,y \mid 0,0) = \frac{kx}{r} H_1^{(2)}(kr) \tag{A.9}$$

$$\frac{1}{\mu} \hat{\sigma}_{xx}^{\psi}(x,y \mid 0,0) = 2xy \left\{ \frac{2k}{r^3} H_1^{(2)}(kr) - \frac{k^2}{r^2} H_o^{(2)}(kr) \right\} \tag{A.10}$$

$$\frac{1}{\mu} \hat{\sigma}_{yy}^{\psi}(x,y \mid 0,0) = -\frac{1}{\mu} \sigma_{xx}^{\psi}(x,y \mid 0,0) \tag{A.11}$$

$$\frac{1}{\mu} \hat{\sigma}_{xy}^{\psi}(x,y \mid 0,0) = -(x^2 - y^2) \left\{ \frac{2k}{r^3} H_1^{(2)}(kr) - \frac{k^2}{r^2} H_o^{(2)}(kr) \right\} \tag{A.12}$$

where $k = \omega/\beta$.

NOTE: To calculate $\hat{u}(x,y \mid x_s,y_s)$ or $\hat{\sigma}(x,y \mid x_s,y_s)$ using the above expressions, replace

(i) x by $(x - x_s)$

(ii) y by $(y - y_s)$

(iii) r by $\sqrt{(x - x_s)^2 + (y - y_s)^2}$.

APPENDIX B

Displacements and Stresses Generated by Line Sources in a Semi-Infinite Elastic Medium

(1) Compressional Wave Source at Point $(x,y) = (0,f)$

$$\hat{\phi}(x,y \mid 0,f) \to H_o^{(2)}(hr) \quad \text{as } r \to 0 \tag{B.1}$$

$$\hat{u}_x^{\phi}(x,y \mid 0,f) = -hx\left[\frac{H_1^{(2)}(hr)}{r} - \frac{H_1^{(2)}(hr_o)}{r_o}\right] + \frac{16i}{\pi}\int_o^{\infty} \frac{kz^3\nu'}{F(z)} e^{-k\nu(f+y)} \sin(kxz)dz - \frac{8i}{\pi}\int_o^{\infty} \frac{kz(2z^2-1)\nu'}{F(z)} e^{-k\nu f} e^{-k\nu' y} \sin(kxz)dz \tag{B.2}$$

$$\hat{u}_y^{\phi}(x,y \mid 0,f) = -h\left[H_1^{(2)}(hr)\,\frac{(y-f)}{r} + H_1^{(2)}(hr_o)\,\frac{(y+f)}{r_o}\right] + \frac{4i}{\pi}\int_o^{\infty} \frac{k(2z^2-1)^2}{F(z)} e^{-k\nu(f+y)} \cos(kxz)dz - \frac{8i}{\pi}\int_o^{\infty} \frac{kz^2(2z^2-1)}{F(z)} e^{-k\nu f} e^{-k\nu' y} \cos(kxz)dz \tag{B.3}$$

$$\frac{1}{\mu}\hat{\sigma}_{xx}^{\phi}(x,y \mid 0,f) = 2h\left[\frac{1}{r} - \frac{2(y-f)^2}{r^3}\right]H_1^{(2)}(hr) + \left[2h^2\,\frac{(y-f)^2}{r^2}\right]H_o^{(2)}(hr) - 2h\left[\frac{1}{r_o} - \frac{2(y+f)^2}{r_o^3}\right]H_1^{(2)}(hr_o) - \left[2h^2\,\frac{(y+f)^2}{r_o^2} - k^2\right]H_o^{(2)}(hr_o) + \frac{16i}{\pi}\int_o^{\infty} \frac{k^2z^2\nu'}{F(z)} e^{-k\nu f}\left\{\left[2z^2 + (1-2n^2)\right]e^{-k\nu y} - (2z^2-1)e^{-k\nu' y}\right\}\cos(kxy)dz \tag{B.4}$$

$$\frac{1}{\mu}\hat{\sigma}_{yy}^{\phi}(x,y \mid 0,f) = 2h\left[\frac{1}{r} - \frac{2x^2}{r^3}\right]H_1^{(2)}(hr) + \left[2h^2\,\frac{x^2}{r^2} - k^2\right]H_o^{(2)}(hr)$$

$$- 2h\left[\frac{1}{r_o} - \frac{2x^2}{r_o^3}\right]H_1^{(2)}(hr_o) - \left[2h^2\frac{x^2}{r_o^2} - k^2\right]H_o^{(2)}(hr_o)$$

$$- \frac{16i}{\pi}\int_o^\infty \frac{k^2z^2(2z^2-1)\nu'}{F(z)} e^{-k\nu f}\{e^{-k\nu y} - e^{-k\nu' y}\}\cos(kxz)dz \qquad (B.5)$$

$$\frac{1}{\mu}\hat{\sigma}_{xy}^{\phi}(x,y \mid 0,f) = \frac{4hx(y-f)}{r^3}H_1^{(2)}(hr) - \frac{2h^2x(y-f)}{r^2}H_o^{(2)}(hr)$$

$$+ \frac{4hx(y+f)}{r_o^3}H_1^{(2)}(hr_o) - \frac{2h^2x(y+f)}{r_o^2}H_o^{(2)}(hr_o)$$

$$- \frac{8i}{\pi}\int_o^\infty \frac{k^2z\,(2z^2-1)^2}{F(z)} e^{-k\nu f}\{e^{-k\nu y} - e^{-k\nu' y}\}\sin(kxz)dz \qquad (B.6)$$

where

$$i = \sqrt{-1}$$

$$\nu = \sqrt{z^2 - \gamma^2}$$

$$\nu' = \sqrt{z^2 - 1}$$

$$F(z) = (2z^2-1)^2 - 4z^2\nu\nu'$$

$$h = \omega/\alpha$$

$$k = \omega/\beta$$

$$\gamma = \beta/\alpha$$

$$r = \sqrt{x^2 + (y-f)^2}$$

$$r_o = \sqrt{x^2 + (y+f)^2}$$

and the source is at $(x,y) = (0,f)$.

(2) Shear Wave Source at Point (x,y) = (0,f)

$$\hat{\psi}(x,y \mid 0,f) \to H_o^{(2)}(kr) \quad \text{as } r \to 0 \tag{B.7}$$

$$\hat{u}_x^{\psi}(x,y \mid 0,f) = -k\left[H_1^{(2)}(kr)\,\frac{(y-f)}{r} + H_1^{(2)}(kr_o)\,\frac{(y+f)}{r_o}\right]$$
$$+ \frac{4i}{\pi}\int_o^{\infty} \frac{k(2z^2-1)^2}{F(z)}\, e^{-k\nu'(y+f)}\cos(kxz)\,dz$$
$$- \frac{8i}{\pi}\int_o^{\infty} \frac{kz^2(2z^2-1)}{F(z)}\, e^{-k\nu' f} e^{-k\nu' y}\cos(kxz)\,dz \tag{B.8}$$

$$\hat{u}_y^{\psi}(x,y \mid 0,f) = kx\left[\frac{H_1^{(2)}(kr)}{r} - \frac{H_1^{(2)}(kr_o)}{r_o}\right]$$
$$- \frac{16i}{\pi}\int_o^{\infty} \frac{kz^3\nu}{F(z)}\, e^{-k\nu'(f+y)}\sin(kxz)\,dz$$
$$+ \frac{8i}{\pi}\int_o^{\infty} \frac{kz(2z^2-1)\nu}{F(z)}\, e^{-k\nu' f} e^{-k\nu y}\sin(kxz)\,dz \tag{B.9}$$

$$\frac{1}{\mu}\hat{\sigma}_{xx}^{\psi}(x,y \mid 0,f) = 4\,\frac{kx(y-f)}{r^3}H_1^{(2)}(kr) - 2\,\frac{k^2x(y-f)}{r^2}H_o^{(2)}(kr)$$
$$+ \frac{4kx(y+f)}{r_o^3}H_1^{(2)}(kr_o) - 2\,\frac{k^2x(y+f)}{r_o^2}H_o^{(2)}(kr_o)$$
$$+ \frac{8i}{\pi}\int_o^{\infty} \frac{k^2z(2z^2-1)}{F(z)}\, e^{-k\nu' f}\Big\{\left[2z^2 + (1-2n^2)\right]e^{-k\nu y}$$
$$- (2z^2-1)e^{-k\nu' y}\Big\}\sin(kxz)\,dz \tag{B.10}$$

$$\frac{1}{\mu}\hat{\sigma}_{yy}^{\psi}(x,y \mid 0,f) = -\frac{4kx(y-f)}{r^3}H_1^{(2)}(kr) + \frac{2k^2x(y-f)}{r^2}H_o^{(2)}(kr)$$
$$- \frac{4kx(y+f)}{r_o^3}H_1^{(2)}(kr_o) + \frac{2k^2x(y+f)}{r_o^2}H_o^{(2)}(kr_o)$$

$$+ \frac{8i}{\pi} \int_0^\infty \frac{k^2 z(2z^2 - 1)^2}{F(z)} e^{-k\nu' f} \left[e^{-k\nu' y} - e^{-k\nu y}\right] \sin(kxz)dz \tag{B.11}$$

$$\frac{1}{\mu} \hat{\sigma}_{xy}^{\psi}(x,y \mid 0,f) = \left(1 - \frac{2x^2}{r^2}\right)\left[\frac{2k}{r} H_1^{(2)}(kr) - k^2 H_o^{(2)}(kr)\right]$$

$$- \left(1 - \frac{2x^2}{r_o^2}\right)\left[\frac{2k}{r_o} H_1^{(2)}(kr_o) - k^2 H_o^{(2)}(kr_o)\right]$$

$$- \frac{16i}{\pi} \int_0^\infty \frac{k^2 z^2(2z^2 - 1)\nu}{F(z)} e^{-k\nu' f}\left[e^{-k\nu' y} - e^{-k\nu y}\right]\cos(kxz)dz \tag{B.12}$$

NOTE: To calculate $\hat{u}(x,y \mid x_s,y_s)$ or $\hat{\sigma}(x,y \mid x_s,y_s)$ using the above expressions, replace

(i) x by $(x - x_s)$

(ii) f by y_s

(iii) r by $\sqrt{(x - x_s)^2 + (y - y_s)^2}$

(iv) r_o by $\sqrt{(x - x_s)^2 + (y + y_s)^2}$

APPENDIX C

Displacements and Stresses Generated by P or SV Incident Waves in a Semi-Infinite Elastic Medium

1) Incident P-Wave:

For a plane P-wave with an angle of incidence of e and an amplitude of |P| (Figure C1), the displacement and stress fields in a semi-infinite medium can be expressed as

$$u_x^{ff}(x,y) = - ihcose[\phi^i(x,y) + \phi^r(x,y)] - ihcosetanf\psi^r(x,y) \tag{C.1}$$

$$u_y^{ff}(x,y) = - ihsine[\phi^i(x,y) - \phi^r(x,y)] + ihcose\psi^r(x,y) \tag{C.2}$$

$$\frac{1}{\mu}\sigma_{xx}^{ff}(x,y) = [2h^2sin^2e - k^2]\,[\phi^i(x,y) + \phi^r(x,y)] - 2h^2tanfcos^2e\psi^r(x,y) \tag{C.3}$$

$$\frac{1}{\mu}\sigma_{yy}^{ff}(x,y) = [2h^2cos^2e - k^2]\,[\phi^i(x,y) + \phi^r(x,y)] + 2h^2tanfcos^2e\psi^r(x,y) \tag{C.4}$$

$$\frac{1}{\mu}\sigma_{xy}^{ff}(x,y) = h^2sin2e[\phi^i(x,y) - \phi^r(x,y)] + [2h^2cos^2e - k^2]\psi^r(x,y) \tag{C.5}$$

where

$$\phi^i(x,y) = A\exp(- ih(xcose - ysine)) \quad , \tag{C.6}$$

$$\phi^r(x,y) = B\exp(- ih(xcose + ysine)) \quad , \tag{C.7}$$

and

$$\psi^r(x,y) = C\exp(- ih(xcose + ytanfcose)) \quad . \tag{C.8}$$

The constants are defined as follows:

$$A = \frac{i}{h} |P| \ , \tag{C.9}$$

$$B = \frac{A}{\Delta} [-(2h^2\cos^2 e - k^2)^2 + 4h^4 \tan f \sin e \cos^3 e] \ , \tag{C.10}$$

$$C = \frac{A}{\Delta} [-2h^2 \sin 2e (2h^2\cos^2 e - k^2)] \ , \tag{C.11}$$

$$\Delta = (2h^2\cos^2 e - k^2)^2 + 4h^4 \tan f \sin e \cos^3 e \ , \tag{C.12}$$

$$h = \frac{\omega}{\alpha} \ , \quad \gamma = \frac{\beta}{\alpha} \ ,$$

and

$$\tan^2 f = \frac{1}{\gamma^2} \tan^2 e + \left(\frac{1}{\gamma^2} - 1\right) \ . \tag{C.13}$$

2) Incidence of SV-Wave:

For a plane SV-wave with an angle of incidence of f and an amplitude of $|s|$ (Figure C2), the displacement and stress fields in a semi-infinite medium can be expressed as

$$u_x^{ff}(x,y) = - ik\cos f \phi^r(x,y) + ik\sin f[\psi^i(x,y) - \psi^r(x,y)] \tag{C.14}$$

$$u_y^{ff}(x,y) = - ik\tan e \cos f \phi^r(x,y) + ik\cos f[\psi^i(x,y) + \psi^r(x,y)] \tag{C.15}$$

$$\frac{1}{\mu} \sigma_{xx}^{ff}(x,y) = [2k^2\tan^2\cos^2 f - k^2]\phi^r(x,y) + 2k^2 \sin f \cos f[\psi^i(x,y) - \psi^r(x,y)] \tag{C.16}$$

$$\frac{1}{\mu} \sigma_{yy}^{ff}(x,y) = [2k^2\cos^2 f - k^2]\phi^r(x,y) - 2k^2 \sin f \cos f[\psi^i(x,y) - \psi^r(x,y)] \tag{C.17}$$

$$\frac{1}{\mu}\sigma_{xy}^{ff}(x,y) = -2k^2\tan e\cos^2 f\phi^r(x,y)$$

$$+ [2k^2\cos^2 f - k^2][\psi^i(x,y) + \psi^r(x,y)] \qquad (C.18)$$

where

$$\psi^i(x,y) = D\exp(-ik(x\cos f - y\sin f)) \quad , \qquad (C.19)$$

$$\psi^r(x,y) = E\exp(-ik(x\cos f + y\sin f)) \quad , \qquad (C.20)$$

and

$$\phi^r(x,y) = F\exp(-ik(x\cos f + y\tan e\cos f)) \quad . \qquad (C.21)$$

The constants are defined as follows:

$$D = -\frac{i|s|}{k} \qquad (C.22)$$

$$E = \frac{D}{\Delta}[-(2k^2\cos^2 f - k^2)^2 + 4k^4\tan e\sin f\cos^3 f] \qquad (C.23)$$

$$F = \frac{D}{\Delta}[4k^2\sin f\cos f(2k^2\cos^2 f - k^2)] \qquad (C.24)$$

$$\Delta = [2k^2\cos^2 f - k^2]^2 + 4k^4\tan e\sin f\cos^3 f \qquad (C.25)$$

$$k = \frac{\omega}{\beta} \quad , \quad \gamma = \frac{\beta}{\alpha}$$

and

$$\tan^2 e = \gamma^2\tan^2 f + (\gamma^2 - 1) \qquad (C.26)$$

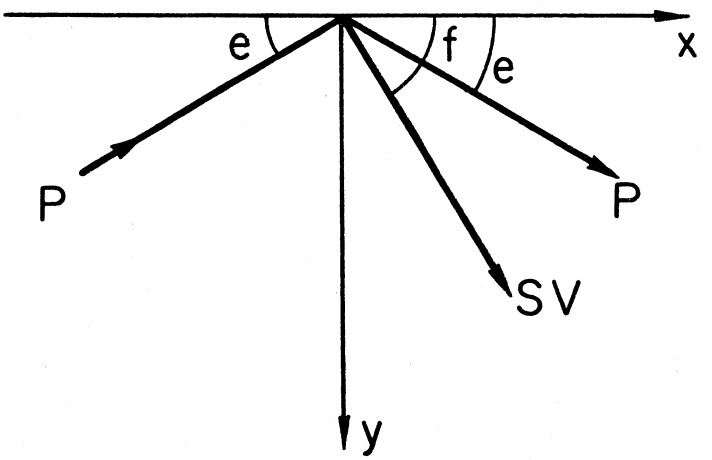

Figure C1

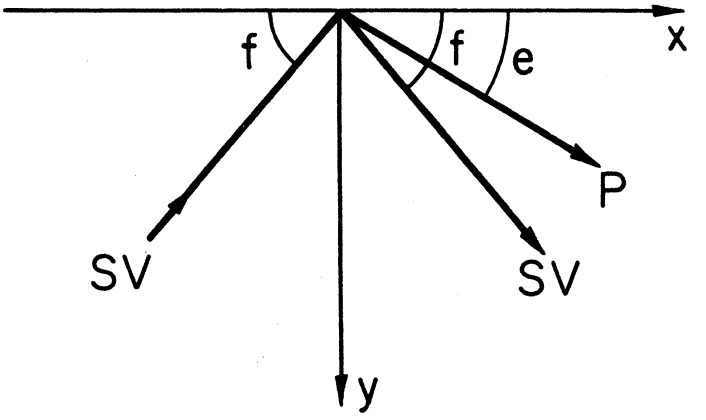

Figure C2

APPENDIX D

Displacements and Stresses Generated by a Rayleigh Wave in a Semi-infinite Elastic Medium

For a Rayleigh wave, the displacement and stress fields in a semi-infinite medium can be expressed as

$$u_x^{ff}(x,y) = De^{-ikx}\left[e^{-\nu_\alpha y} - \frac{1}{2}\left[2 - \frac{c^2}{\beta^2}\right]e^{-\nu_\beta y}\right]$$

$$u_y^{ff}(x,y) = iDe^{-ikx}\left[-\sqrt{1 - \frac{c^2}{\alpha^2}}\, e^{-\nu_\alpha y} + \frac{\left[2 - \frac{c^2}{\beta^2}\right]}{2\sqrt{1 - \frac{c^2}{\beta^2}}} e^{-\nu_\beta y}\right]$$

$$\frac{1}{\mu}\sigma_{xx}^{ff}(x,y) = ikDe^{-ikx}\left[\left(-3 + 2\frac{c^2}{\alpha^2}\right)e^{-\nu_\alpha y} + \left(2 - \frac{c^2}{\beta^2}\right)e^{-\nu_\beta y}\right]$$

$$\frac{1}{\mu}\sigma_{yy}^{ff}(x,y) = ikDe^{-ikx}\left[e^{-\nu_\alpha y} - \left(2 - \frac{c^2}{\beta^2}\right)e^{-\nu_\beta y}\right]$$

$$\frac{1}{\mu}\sigma_{xy}^{ff}(x,y) = De^{-ikx}\left[-2\nu_\alpha e^{-\nu_\alpha y} + \frac{k^2\left[2 - \frac{c^2}{\beta^2}\right]}{2\nu_\beta} e^{-\nu_\beta y}\right]$$

where

$$\nu_\alpha = k\sqrt{1 - \frac{c^2}{\alpha^2}}$$

$$\nu_\beta = k\sqrt{1 - \frac{c^2}{\beta^2}}$$

and c/β is the root of the equation

$$\left(\frac{c}{\beta}\right)^6 - 8\left(\frac{c}{\beta}\right)^4 + \left(24 - 16\,\frac{\beta^2}{\alpha^2}\right)\left(\frac{c}{\beta}\right)^2 - 16\left(1 - \frac{\beta^2}{\alpha^2}\right) = 0 \quad .$$